Part IV

CHEMICAL AND TOPOLOGICAL ORDER IN SHEAR BANDS

Although a number of simulation studies on the atomics structure of metallic glasses, and shear bands in particular, was published in the past 10 years [59, 61, 69, 136, 137], it is still difficult to connect simulation results with experimental findings. In the previous chapter we observed that in the case of Cu-rich Cu-Zr glasses, plastic deformation involves the destruction of Cu-centered FI clusters, which is in good agreement with recent simulation studies. It was suggested that these FI-units form a percolating structural backbone being a pre-requisite for strain localization [32]. This picture, however, has been questioned [33] and up to now it was not possible to distinguish which structural defects actually lead to shear localization and which defects are caused by plastic deformation. In this part, we first characterized the chemical and topological order in shear bands and subsequently investigated the recovery of shear bands under thermal annealing.

7

STRUCTURAL CHARACTERIZATION OF SHEAR BANDS

In this chapter, we take a closer look at the structural defects introduced by plastic deformation. We characterize two glasses of different alloy composition, the Cu-rich $Cu_{64}Zr_{36}$ glass already discussed in the previous chapter, and a Zr-rich $Cu_{36}Zr_{64}$ glass. Both glasses were deformed at 50 K by applying a constant strain rate of $4 \cdot 10^7\,s^{-1}$ with open boundaries in one dimension and periodic boundaries in the others. In particular, we address the following questions: (i) Is the chemical short range order affected by plastic deformation and, if yes, how? (ii) Are the changes in topological short range order in a $Cu_{36}Zr_{64}$ glass similar to what we have observed for the $Cu_{64}Zr_{36}$ glass in Section 5.3? (iii) How is the medium range order damaged during plastic deformation? (iv) Is it possible to discriminate which defects lead to strain localization and which defects are caused by shear banding?

7.1 STRESS-STRAIN BEHAVIOR

When loaded in uniaxial tension, the Cu-rich as well as the Zr-rich glass deform by shear banding as shown in Fig. 57(b) and (c). According to the stress-strain curves (Fig. 57(a)), the stress required for SB formation in $Cu_{64}Zr_{36}$ and the subsequent stress drop is significantly higher than in $Cu_{36}Zr_{64}$. While for the Cu-rich alloy SB formation starts immediately after the maximum stress is reached, we find about 4% homogeneous plastic strain for the Zr-rich alloy prior to shear banding,which is reflected in the constant stress between 6% and 10% strain.

In the following we will characterize the structural defects occurring during deformation and relate them to the macroscopic deformation behavior.

7.2 CHEMICAL SHORT RANGE ORDER

In order to see how the changes in CSRO evolve during deformation, we have calculated the correlation indices C_{ij} (with $i, j =$ Cu, Zr), for a test volume inside the shear band and in the surrounding matrix, and monitored their changes during deformation. The resulting data are displayed in Fig. 35. For both glassy

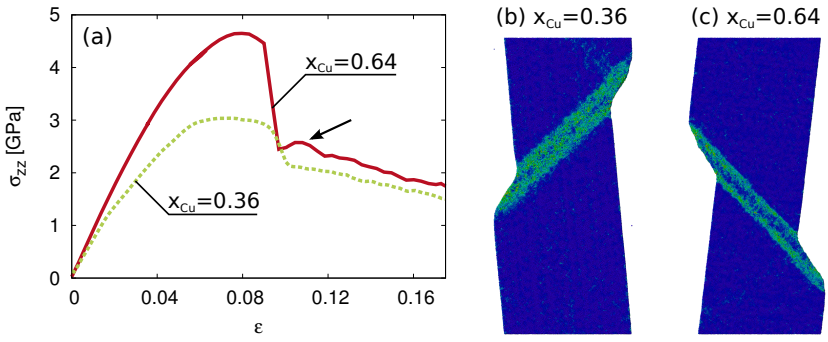

Figure 34: (a) Stress-strain curves for metallic glasses under tensile deformation. In the (b) $Cu_{64}Zr_{36}$ glass as well as in the (c) $Cu_{36}Zr_{64}$ glass plastic deformation occurs highly localized in one dominant shear band.

alloys the CSRO in the matrix (green) is hardly affected by deformation. In the region where the SB forms (red), however, we observe significant changes which are similar for both glasses. At the strain where SB nucleation occurs (see dashed lines in Fig. 35), we observe a steep increase in C_{CuCu} and C_{ZrZr} and a decrease in C_{CuZr} indicating that the number of Cu-Cu- and Zr-Zr-bonds grows at the expense of unlike Cu-Zr-bonds. Interestingly, for the Cu-rich alloy we find a stronger increase in the fraction of Zr-Zr bonds than in the number of Cu-Cu bonds, while we observe the opposite trend for the Zr-rich alloy. These changes persist during SB slip up to higher strains and no steady state is reached where the CSRO is stable, only the slopes of the curves decrease.

Independent of the alloy composition, plastic deformation leads to an increase in the fraction of Cu-Cu- and Zr-Zr-bonds and a decrease in the fraction of Cu-Zr-bonds. In the surrounding matrix, the CSRO is hardly affected.

7.3 TOPOLOGICAL SHORT RANGE ORDER

For characterizing the atomic scale mechanisms involved in shear banding, we have analyzed local changes in Voronoi volume and topological short range order upon deformation. Particularly, the fraction of Cu-atoms coordinated in FIs and their distribution in the sample are monitored. We have, therefore, scanned the average Voronoi volumes and the fraction of Cu-centered FIs for snapshots at different strains during tensile deformation (see Fig. 36). Since the evolution of Voronoi volumes around Cu- and Zr-atoms is similar, only the Voronoi volumes of Cu-atoms are given in Fig. 36 (a) and (c). For the case of the $Cu_{64}Zr_{36}$ glass (Fig. 36 (a,b)), the evolution of the TSRO was already discussed in Chapter 5. For better comparison of the two alloys studied in this chapter, the findings will be recapitulated here: Up to a strain of about 8% the atomic volumes increase linearly

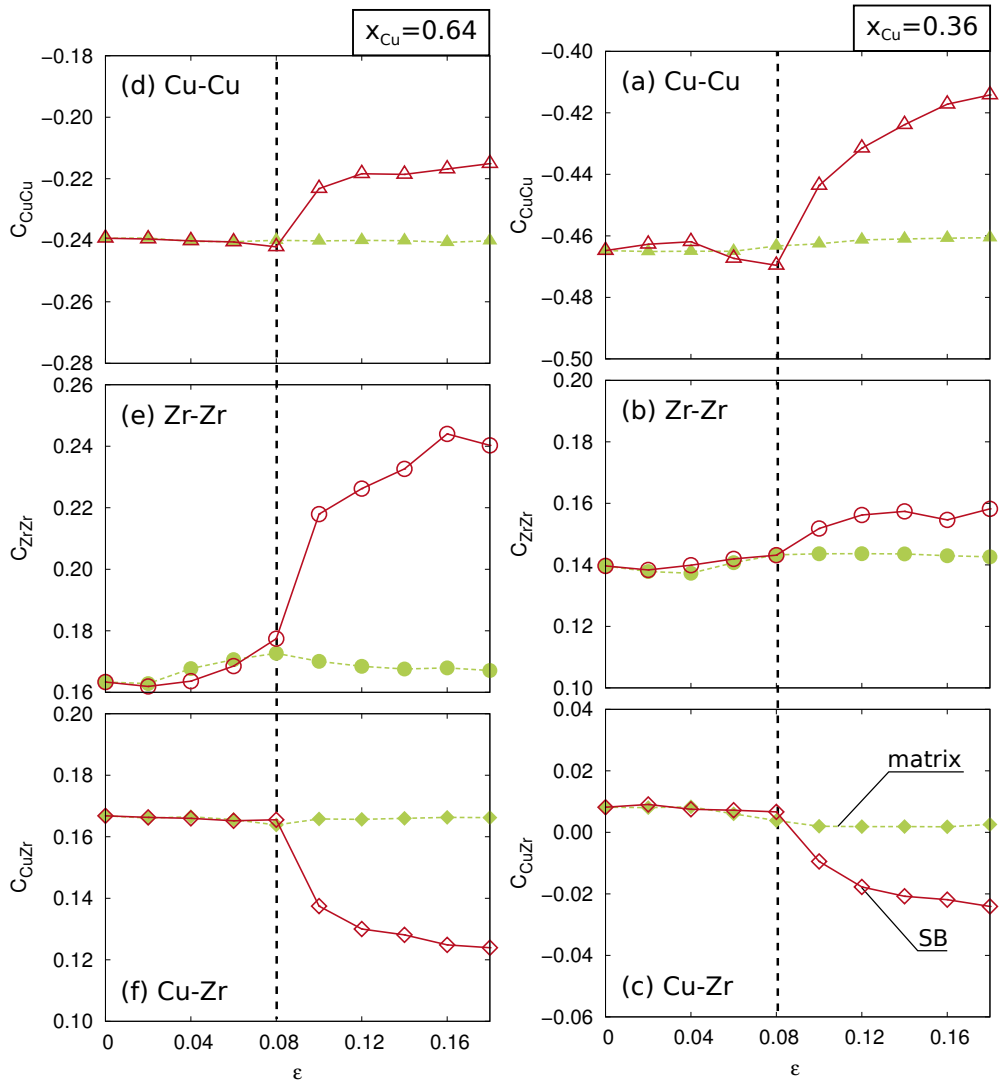

Figure 35: Changes in CSRO during tensile deformation in both glassy alloys measured by the variation in the nearest neighbor correlation indices C_{ij} (with $i, j =$ Cu, Zr). The C_{ij}-values were calculated for a test volume inside the SB and in the surrounding matrix.

and homogeneously in the whole sample, while the FI occupation decreases slowly in the whole sample from 22% in the virgin sample to 19.5%. Between 8% and 9% strain a SB forms at the surface which has penetrated the whole sample at a strain of 9.4%, the point when SB-slip sets in. Inside the SB free volume is generated which is seen as an increase of the average Voronoi volumes at the position of the SB at $x = 0$ (Fig. 36 (a)). At the same time, the atomic volumes in

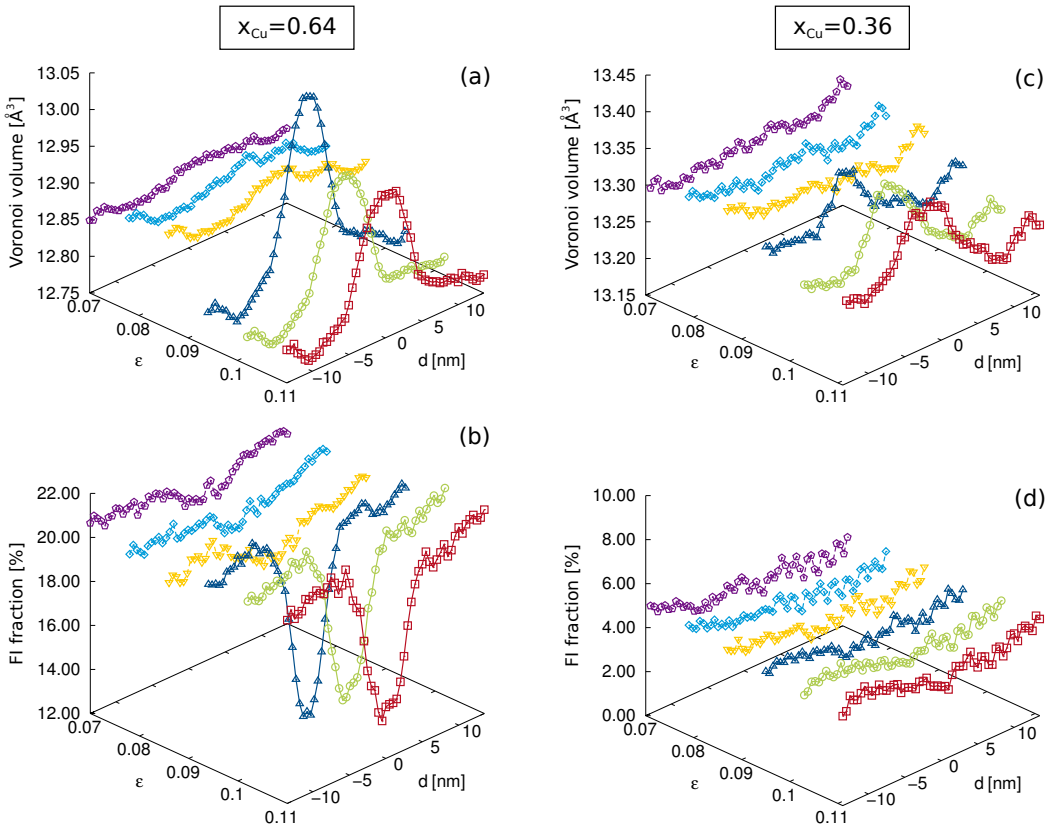

Figure 36: Linear scans of (a,c) the average Voronoi volume around Cu-atoms, and (b,d) the fraction of Cu-centered full icosahedra at different strains during deformation of a (a-b) $Cu_{64}Zr_{36}$ and a (c-d) $Cu_{36}Zr_{64}$ glass.

the undeformed matrix decrease as a result of a compressive stress component introduced by the volume expansion of the shear band. The TSRO in the matrix is hardly affected since all deformation occurs localized inside the shear band, and the occupation of Cu-centered full icosahedra remains constant. SB-slip enables structural relaxations inside the SB and leads to a recovery of the atomic structure, namely a decrease in free volume and an increase in FI-density. This relaxation effect can also be seen in the corresponding snapshot in Fig. 57(c), where the structural recovery inside the SB is visible as a less strained region.

To check whether these observations are transferable to different alloy compositions, we have performed the same analysis for the $Cu_{36}Zr_{36}$ glass under tensile deformation (Fig. 36 (c,d)). Analogous to the Cu-rich alloy, we find increased Voronoi volumes inside the shear band (Fig. 36 (c)), but the dilatation is not as pronounced in the case of the Zr-rich glass. Again, the surrounding matrix is compressed. Surprisingly, the FI-density is not affected by SB formation at all

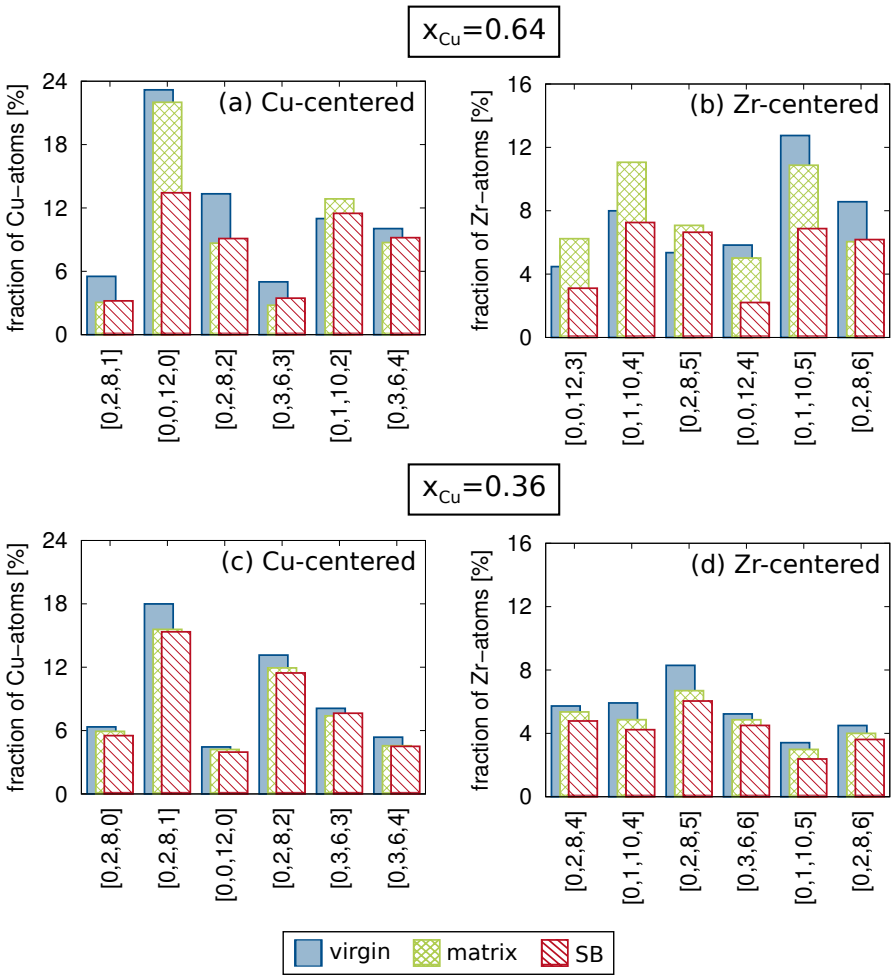

Figure 37: Population of Cu- and Zr-centered Voronoi polyhedra in (a,b) Cu-rich and (c,d) Zr-rich metallic glass for the undeformed material, inside a shear band and in the surrounding matrix. Only VPs with an initial population of more than 3% are considered.

(Fig. 36 (d)). Comparing the undeformed glasses, we find that the population of Cu-centered FIs in the Cu-rich alloy is about 22% compared to only 5% in the Zr-rich alloy. In literature, it was reported that the FI-clusters with high packing density and high shear resistance determine the plasticity of Cu-Zr glasses [45] and that the variation in FI-density with the Cu-content is responsible for the corresponding variation in yield stress and plastic strain [32]. It was suggested that metallic glasses derive their exceptional strength from a percolating backbone of SRO-clusters, which has to be destroyed to enable yielding [57]. Consequently, in case of the Cu-rich glass with high FI-density the material can only flow if the

structural backbone is ruptured at sufficiently high stress, as observed inside the SB. For the Zr-rich glass we did not observe the breakdown of icosahedral SRO and the yield stress is about 1.7 GPa lower as compared to the $Cu_{64}Zr_{36}$ glass (see stress-strain curves in Fig. 35). There are three candidates to explain this behavior: (a) The Cu-centered full icosahedron is not the relevant topological feature in this material and the structural backbone consists of different SRO-clusters with lower shear resistance leading to a lower yield stress. (b) Although the total FI-fraction in the Zr-rich glass appears to be constant, FI clusters could still be destroyed during plastic deformation if the recovery of FIs occurred with a similar rate. This explanation is based on a study by Lekka *et al.* [138] who claim that the deformation of a $Cu_{46}Zr_{54}$ glass involves the continuous creation and destruction of Cu-centered FI clusters resulting in a dynamically constant population of FIs. (c) A $Cu_{36}Zr_{64}$ glass simply does not have a percolated backbone since the individual FIs are further separated and not interconnected. This would also be reflected in a low yield stress and could explain why we do not see a decrease in FI-density in this material upon yielding.

Concerning point (a) we wanted to clarify whether there is any characteristic SRO-cluster in $Cu_{36}Zr_{64}$ glass other than the Cu-centered full icosahedron. We have, therefore, identified Voronoi polyhedra with a population of more than 3% which are shown in Fig. 37 for both alloys in the undeformed state (blue) and after deformation in SB (red) and surrounding matrix (green). The population of VPs in the Cu-rich glass (Fig. 37 (a,b)) supports the picture of a FI-backbone that is damaged in the SB, while the surrounding material is hardly affected: the fraction of Cu-centered clusters with index [0,0,12,0] in the matrix hardly deviates from the virgin material and inside the SB the FI-fraction is roughly half the initial value. Changes in the population of other VPs are less pronounced compared to the change in FI-fraction, but the fraction of Zr-centered clusters with index [0,0,12,3], [0,1,10,4], [0,0,12,4], and [0,1,10,5] is decreased by several percent in the SB with respect to the virgin material. Like the full icosahedron, these clusters are characterized by a large number of pentagonal facets, which are indicative of dense atomic packing and high shear resistance [45]. Hence, for the example of $Cu_{64}Zr_{36}$ glass we clearly see that densely packed regions with high shear resistance are destroyed to enable yielding.

In the undeformed $Cu_{36}Zr_{64}$ glass (Fig. 37 (c,d)), the most prominent topological features are Cu-centered clusters with index [0,2,8,1] as well as clusters with index [0,2,8,2]. The first kind of clusters are present in $Cu_{64}Zr_{36}$ glass with a much lower frequency, while the latter VP occurs with similar frequency. If our first hypothesis of a new characteristic SRO-cluster was correct, we would expect the population of these clusters to be significantly decreased inside the SB. Comparing the population of atomic clusters in SB, matrix and virgin glass, however, we find that the differences are by far less pronounced than in the Cu-rich glass. Moreover, the values for SB and surrounding matrix are almost identical for

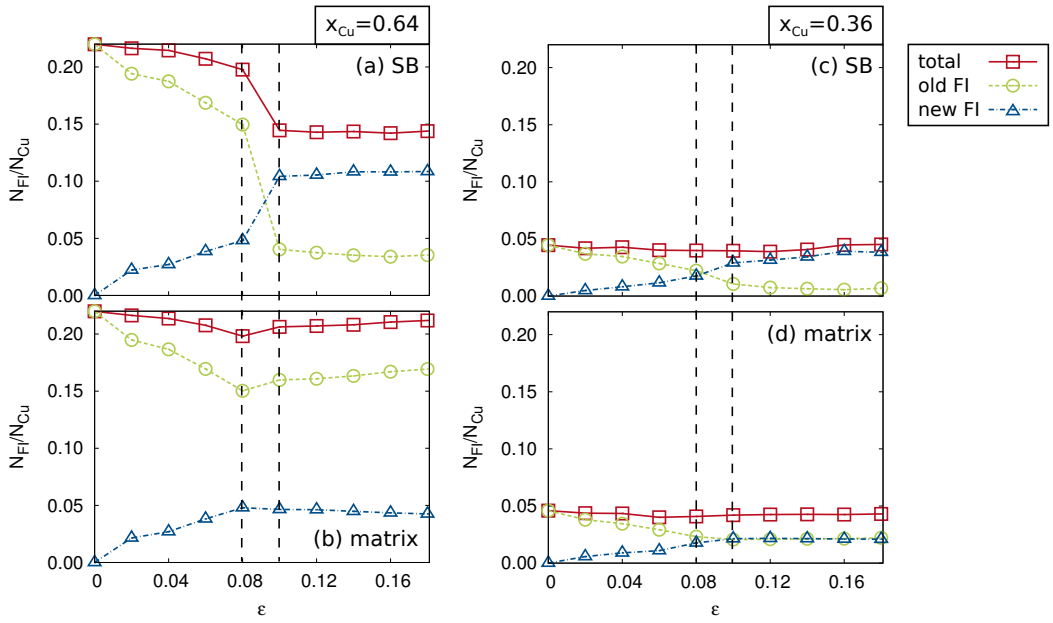

Figure 38: Evolution of the total number of FI clusters in addition to the destruction and creation of Cu-centered FI clusters during tensile deformation with respect to the number of Cu-atoms: (a) in the SB and (b) in the matrix of the Cu-rich alloy; (c) in the SB and (d) in the matrix of the Zr-rich alloy.

all VPs considered in our analysis, indicating that there actually is no other SRO-cluster forming a backbone which is destroyed in the SB.

Next, we investigate the evolution of icosahedral clusters during plastic deformation with regard to point (b) to elucidate the interplay of destruction and creation of FIs. Fig. 38 shows the evolution of the total number of FI clusters with respect to the number of Cu-atoms (=total; red), in addition to the number of FIs which were already present in the original glass structure (=old FI; green) and the number of newly created FIs (=new FI; blue), in both alloys for SB and surrounding matrix. Up to a strain of 8%, before strain localization sets in in either of the samples, we observe the same behavior in the SB and matrix region. The total fraction of FIs in the Cu-rich alloy (Fig. 38 (a) and (b)) decreases from 22% to 20% resulting from the destruction of almost one third of the original FI-clusters which is not fully compensated by newly created FIs. In the Zr-rich glass (Fig. 38 (c) and (d)) on the other hand, the total number of FIs remains constant, since new FIs are created at the same rate as the initial FIs are destroyed. At 8% strain about half of the FI-clusters that were present in the initial sample are destroyed.

When a SB forms between 8% and 10% strain, the total FI-fraction in the SB region drops from 20% to 15% for the case of the Cu-rich alloy (Fig. 38 (a)). Only

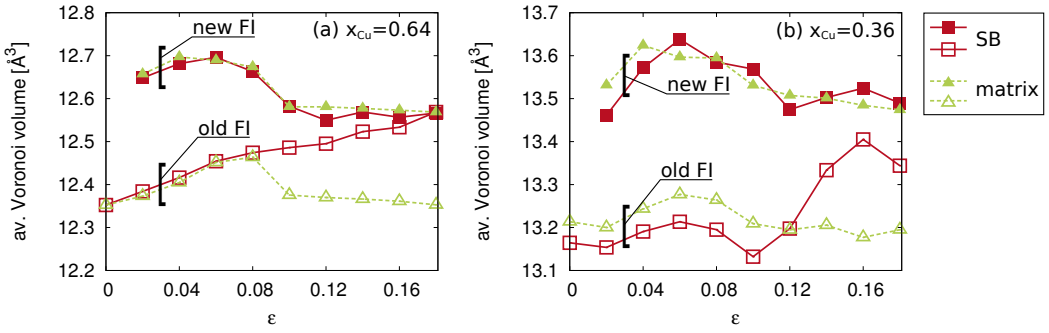

Figure 39: Evolution of average Voronoi volumes of FIs remaining from the original SRO (=old FI) and newly formed FIs (=new FI) in SB and matrix during deformation (a) for the Cu-rich glass and (b) for the Zr-rich glass.

about 20% of the FI clusters remaining from the original SRO are unaffected and although the recovery of FIs appears to be enhanced inside the SB, as well, we find a decrease in the total number of FIs. In the matrix, the total number of FIs slightly increases when the SB forms. This is attributed to the release of elastic strain in the material surrounding the SB leading to an increase in the number of original FI clusters. The creation of new FIs does not contribute to the increase in the total number of FIs in this regime. In the Zr-rich alloy, shear banding also occurs between 8% and 10% strain. Here, the total number of FIs is actually constant, in SB and matrix, which is in agreement with Fig. 36(d). Analyzing the number of remaining original FI clusters we find, however, that almost all original FI-clusters are destroyed during SB formation. But this decrease in the FI density is fully compensated by the creation of new FIs. In the matrix we hardly detect the destruction or generation of FIs.

For strains higher than 10%, when all deformation is confined in the SB, the total number of FI clusters remains constant in SB and matrix in both samples. We do not observe a further decrease in the number of remaining original FIs and the number of new FIs with respect to the initial glass structures appears constant. In order to learn more about the dynamics of the creation and destruction of FI clusters, we determined how many FIs are created and destroyed within time intervals of 0.5 ns during deformation by comparing successive snapshots. This analysis reveals that although the data in Fig. 36 suggest that no FIs are created or destroyed for strains higher than 10%, the number of new FIs is determined by a dynamic equilibrium. While the rate for the creation and destruction of FIs is low in the matrix, we find 4 and 10-times increased rates inside the SB in the Zr-rich and Cu-rich glass, respectively. So while the remaining original FI-clusters are stable and not affected by further deformation, the newly formed FIs are prone to be destroyed again.

To determine whether the observations discussed above can be related to the volume expansion in shear bands, we calculated the average Voronoi volumes of FIs remaining from the original SRO and newly formed FIs and monitored their evolution during deformation (Fig. 39). Before shear banding sets in, the average Voronoi volume of atoms located in original FI clusters is significantly lower than the Voronoi volume of atoms in new FI clusters for both glassy alloys, the difference being even more pronounced in case of the Zr-rich glass (Fig. 39 (b)). After SB formation, at strains higher than 10%, the average volume of new FIs in the SB increases and in the Cu-rich alloy the difference between old and new FIs almost vanishes with further deformation. In the Zr-rich alloy, however, we still find a significant difference in the average volume of old and new FIs inside the SB, even at 18% strain. The flow dilatation observed in the Zr-rich glass can, therefore, be attributed to the destruction of the original SRO.

In summary, we found that SB-formation in a $Cu_{36}Zr_{64}$ glass leads to the formation of free volume inside the SB similar to the case of a $Cu_{64}Zr_{36}$ glass. Other than in the Cu-rich glass, however, this increase in free volume at first glance appeared not to be related to the destruction of densely packed FI-clusters. Applying the Voronoi analysis we could rule out that there is a different characteristic topological feature with similarly high packing density that is destroyed upon yielding. Analyzing the evolution and destruction of FI clusters we observed that in both glassy alloys the original icosahedral SRO is destroyed in the SB. The destruction of FIs, however, is compensated by the simultaneous recovery of FI clusters. In the Zr-rich alloy the creation of new FIs fully compensates the destruction of the initial FI clusters, while in the Zr-rich alloy the creation of FIs can only account for a partial recovery of the TSRO. The flow dilatation in the SB observed in the Zr-rich glass can be explained by the destruction of the original SRO, since the newly formed FI clusters are characterized by a lower packing density than the original FI clusters.

In the next section we will focus on the medium range order of the two glassy alloys and try to gain more insight in the nature of the structural backbone of interconnected FI-clusters in different Cu-Zr glasses and its role for plastic deformation.

7.4 MEDIUM RANGE ORDER

As previously reported by Lee *et al.*,[46] the medium range order in the Cu–Zr-glasses studied here can be characterized in terms of strings or networks of volume-sharing SRO-clusters, namely Cu-centered icosahedra. Depending on the alloy composition, the size n_{MRO} of these MRO-clusters varies, as well as the degree of cross-linking, which we characterize by the number of neighboring icosahedra N_{FI}, *i.e.*, how many neighbors in the first coordination shell are also centers of other icosahedra. For the case of the Zr-rich glass with low FI-density,

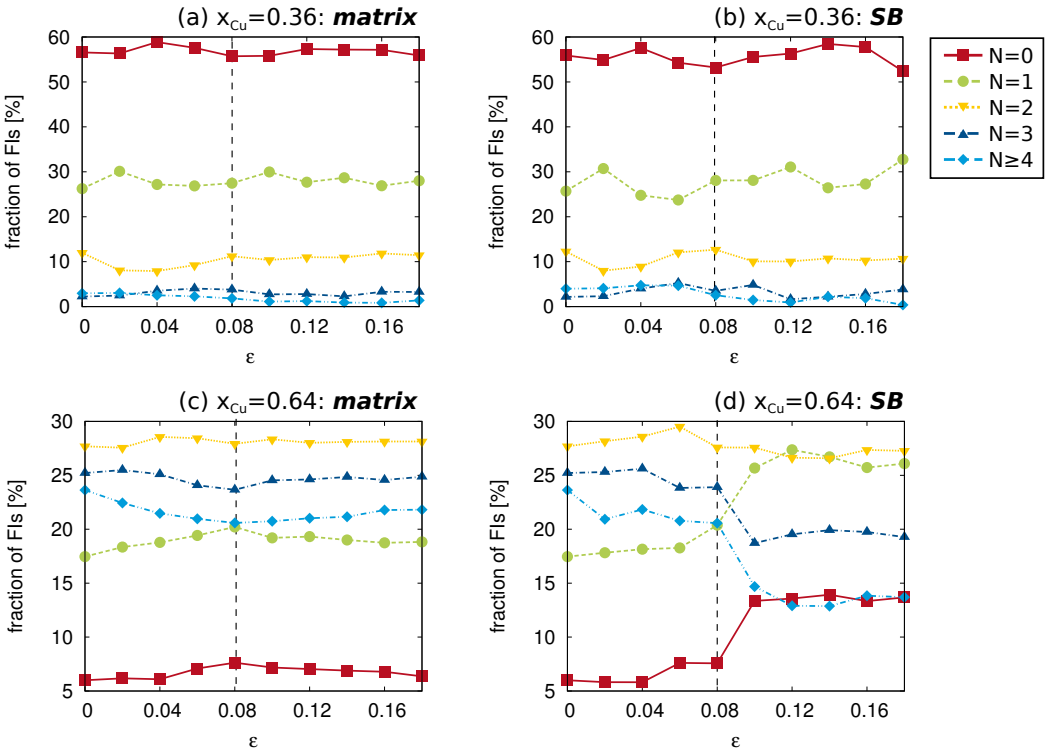

Figure 40: Changes in cross-linking between FI-units during tensile deformation for a (a,b) $Cu_{36}Zr_{64}$- and a (c,d) $Cu_{64}Zr_{36}$ glass : Fraction of FI-units with a certain number of FI-neighbors N_{FI} measured for a test volume inside the SB and in the surrounding matrix as a function of the applied strain.

the average number of icosahedral units per MRO-cluster is $n^{av}_{MRO} = 1.4$ in the undeformed material and about 55% of the FIs are non-interpenetrating FIs ($N_{FI} = 0$). In the Cu-rich glass on the other hand, we find on average 7.1 icosahedral units per MRO-cluster and the degree of cross-linking is significant with only 6% of non-interpenetrating FIs.

Firstly, we have analyzed the changes in cross-linking during deformation by evaluating the fraction of FIs with a certain number of FI-neighbors N_{FI} at different strains, again for a test volume inside the SB and in the surrounding matrix (see Fig. 40). In agreement with the results for the Zr-rich glass discussed in the previous section, where we did not observe variations in the FI-density upon plastic deformation, the number of FI-neighbors remains the same as in the undeformed state, in the SB as well as in the matrix (Fig. 40(a) and (b)). In the Cu-rich alloy, however, we clearly see the effect of plastic deformation on the FI-network: In the matrix the changes are less pronounced, yet, a systematic increase in the fraction of FIs which are non-interpenetrating or have only one

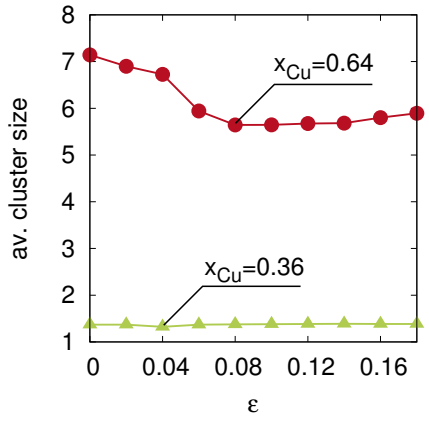

Figure 41: Changes in the average size of MRO-clusters n_{av}, which is the average number of FI-units per MRO-cluster, during deformation.

FI-neighbor ($N_{FI} <= 1$) is obvious together with a decrease in the fraction of FIs with $N_{FI} >= 3$ for strains higher than 4% (see Fig. 40(e)). At about 8% strain, which is the strain at which a SB forms, the trend is reversed due to the recovery of MRO since from that point on all plasticity is localized in the SB. When a SB forms, the changes are more substantial. Apart from the strong decrease in the FI-density observed in the previous section, for strains between 8% and 10% the fractions of FIs with $N_{FI} = 0$ and $N_{FI} = 1$ each increase by about 5%-points. While the fraction of FIs with $N_{FI} = 2$ decreases only slightly, the fraction of FIs with more than 2 FI-neighbors decreases significantly. In other words, MRO-clusters with densely packed interpenetrating icosahedra are disrupted and single ($N_{FI} = 0$) or double ($N_{FI} = 1$) FI-clusters are formed. Moreover, the increase in the fraction of clusters with $N_{FI} = 1$ includes the FIs located at the end of a chain, which form when a longer chain is cut into pieces. After the SB has penetrated the whole sample at a strain of approximately 10%, the fractions of FIs with a certain N_{FI} remain constant indicating a steady state flow regime. This, however, does not mean that the remaining FI-network is stable and not affected by further deformation. Instead, as observed by Lee and co-workers [139], plastic flow inside the SB involves the constant destruction and recovery of MRO-clusters, which is in equilibrium in the steady state flow regime.

The trends described above are also reflected in the variation of the average size of MRO-clusters during deformation (see Fig. 41). While the average cluster size does not change at all in case of the $Cu_{36}Zr_{64}$ glass, the average number of FIs per cluster decreases from 7.1 to 5.6 in the $Cu_{64}Zr_{36}$ glass. Since we have only determined the n^{av}_{MRO} for the whole sample, we expect the effect to be even more pronounced inside the shear band. Interestingly, the decrease in n^{av}_{MRO} occurs at strains below 8%, *i.e.*, before the SB forms. This could mean that the

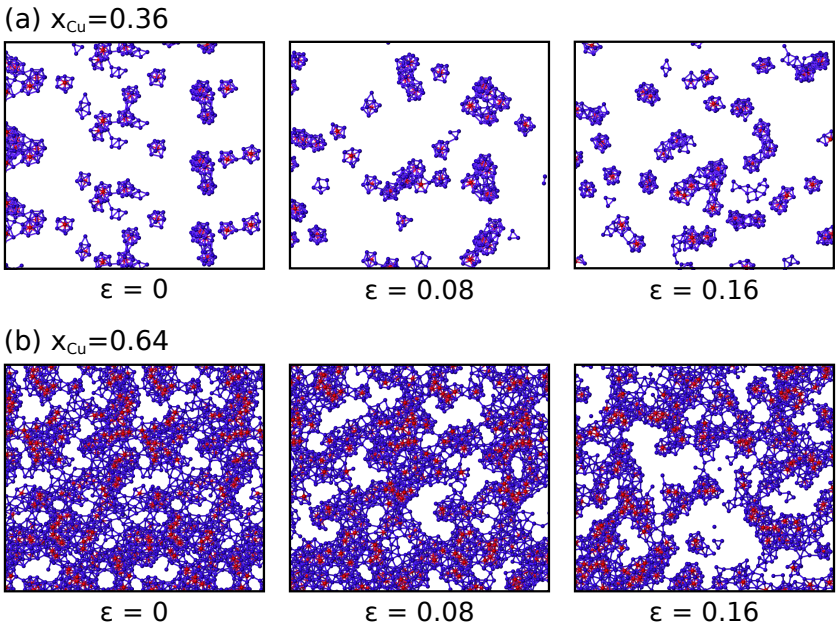

Figure 42: Evolution of MRO-clusters during deformation inside a shear band in (a) a $Cu_{36}Zr_{64}$ glass and (b) a $Cu_{64}Zr_{36}$ glass: For better illustration only the clusters in a slice of the thickness of one FI-unit is displayed; the sections are chosen inside a shear band and the size of the boxes is 9x8 nm^2. Red atoms represent FI-centers and blue atoms are located in their first coordination shell.

disruption of MRO-clusters locally destabilizes the structure of a $Cu_{64}Zr_{36}$ glass and is, therefore, one possible prerequisite for strain localization. Then again, the Zr-rich glass also deforms by shear banding, even if SRO and MRO appear to be hardly affected.

In order to visualize the findings discussed above, we have taken snapshots of the evolution of icosahedral clusters inside the SB during deformation (Fig. 42); for clarity, only the FI-clusters within a slice of the thickness of one FI are displayed. In line with the quantitative analysis, the snapshots demonstrate that in the case of the Zr-rich alloy (Fig. 42(a)), neither the number nor the distribution or cross-linking of the FI-clusters is affected by plastic deformation. For the case of the Cu-rich glass (Fig. 42(b)) we clearly see how the density of FIs decreases along with the disruption of highly interconnected clusters.

7.5 SUMMARY

To conclude this chapter we go back to the questions posed in the introductory paragraph to see whether our study on structural defects inside SBs could provide adequate answers.

(i) *Is the chemical short range order affected by plastic deformation and, if yes, how?* - In both glasses investigated here, we found the CSRO to be affected inside the SB while the surrounding matrix is hardly affected. Independent of the alloy composition, plastic deformation inside the SB leads to an increase in the fraction of Cu-Cu- and Zr-Zr-bonds and a decrease in the fraction of unlike Cu-Zr-bonds.

(ii) *Are the changes in TSRO in $Cu_{36}Zr_{64}$ glass similar to defects in $Cu_{64}Zr_{36}$ glass?* - Similar to the case of the Cu-rich glass we found that SB-formation in the Zr-rich glass leads to an increase in free volume inside the SB. While in the Cu-rich glass we identified the decrease in the total number of densely packed FI clusters inside the SB to be most relevant for the dilatation, the total number of FIs is constant in the Zr-rich glass. Here, the destruction of the original icosahedral SRO is fully compensated by newly formed FI clusters. These new FIs, however, show a lower packing density than the original FIs, which leads to a volume expansion inside the SB. By studying the population of other types of atomic clusters we could rule out that there is a different topological feature with high packing density which is responsible for the shear stability of $Cu_{36}Zr_{64}$ glass and is destroyed upon yielding.

(iii) *How is the medium range order damaged during shear banding?* - We have analyzed the evolution of MRO-clusters built from interpenetrating FIs during deformation, specifically, the degree of cross-linking and the average cluster size. For the Cu-rich alloy we found that together with an absolute decrease in the number of FIs, the degree of cross-linking decreases when a SB forms indicating that highly interconnected clusters are disrupted. The average size of the MRO-clusters decreases even before SB-formation which indicates that the breakdown of the MRO-network is one possible prerequisite for structural destabilization and strain localization. Yet, in the Zr-rich glass, where the FI-density as well as the degree of cross-linking between FI-units is substantially decreased with respect to the Cu-rich glass, the MRO-clusters are hardly affected during deformation. But still, the glass deforms by shear banding.

(iv) *Is it possible to discriminate which defects lead to strain localization and which defects are caused by shear banding?* - Taking into account the results presented here, we still cannot identify the process/es leading to shear localization in Cu-Zr glasses. The observed changes in CSRO as well as the TSRO and MRO (with the exception of the decrease in the average MRO-cluster size in $Cu_{64}Zr_{36}$ glass) occurred during SB formation and/or SB slip and are, therefore, a result of plastic deformation. Consequently, we assume that the concept of a structural backbone of interpenetrating FI-units, which is locally destabilized causing strain localization in a SB, is not appropriate to describe the plasticity of Cu-Zr glasses.

8

MECHANISMS OF SB RECOVERY UNDER THERMAL ANNEALING

The highly deformed material inside a shear band acts like a second phase with lower density, lower elastic modulus and yield strength [81, 82], and an increased diffusivity [140]. Due to the limited atomic mobilities at ambient conditions, shear bands still contain a frozen amount of excess volume after the applied stress is removed [95] and remain weak points in a deformed metallic glass sample. When annealed at elevated temperatures (below the glass transition temperature T_g), however, shear bands recover substantially by annihilation of the excess volume and relaxation of the short range order [141, 142, 95, 140, 143, 144], wherefore the strain softening due to plastic deformation is reversed [140]. After annealing, however, pre-deformed and recovery-annealed samples still exhibit an enhanced ductility as compared to the virgin material [143] and preferential etching is still observed for the relaxed shear bands [95]. One possible explanation for the incomplete recovery is that structural relaxation only requires diffusion distances of less than an atomic diameter, whereas the re-establishment of chemical order requires long range diffusion, which is not achieved under the given annealing conditions [95]. This assumption, however, is contradictory to earlier reports stating that changes in the chemical short range order require only minor changes of the local chemical surroundings, whereas changes in the topological short range order require larger rearrangements [145, 142].

In the framework of free volume theory it appears rather surprising that shear bands do not recover instantaneously when subjected to thermal annealing at high temperatures: An increase in free volume, as observed in shear bands, is related to an increase in fictive temperature and, consequently, a decrease in the viscosity of the glass [146]. At high temperature, the local atomic mobilities and relaxation times should, therefore, be equivalent to mobilities and relaxation times in the supercooled liquid leading to fast recovery of structural defects. This, however, disagrees with experimental observations, where the recovery of deformed samples at high temperature occurs on time scales in the range of hours. This inconsistency asks for a detailed investigation on thermal annealing of plastically deformed metallic glasses to elucidate the atomic scale mechanisms involved in structural relaxation.

In this chapter, we study the annealing behavior of a pre-deformed $Cu_{64}Zr_{36}$ glass at different temperatures below and above T_g. In particular the atomic scale diffusional mechanisms driving the recovery are analyzed in detail.

8.1 SIMULATION DETAILS

For studying the recovery of shear bands in pre-deformed metallic glass during thermal annealing, we have performed classical MD simulations. We have simulated uniaxial tensile deformation of a 3 dim.-periodic sample (36x8x26 nm^3; 432,000 atoms) by applying a constant strain rate of $4 \cdot 10^7$ s^{-1} in z-direction at a constant temperature of 50 K. The pressure in x- and y-direction was kept at 0 kbar allowing for lateral contraction. At a strain of 14%, after one extended shear band had formed, the sample was unloaded to zero stress. The previously deformed and unloaded sample was then heated with a rate of 0.1 K/ps, annealed for 20 ns at 500 K ($\approx 0.55T_g$), 800 K ($\approx 0.85T_g$), and 1000 K ($\approx 1.05T_g$), and subsequently quenched to 50 K, again, using a rate of 0.1 K/ps. For comparison, an as-prepared $Cu_{64}Zr_{36}$ glass sample (8x5x12 nm^3; 32,000 atoms) was subjected to the same thermal treatments.

The short range order and packing density were analyzed using the Voronoi tessellation method. As discussed before, the Cu-centered full icosahedra is a key structural motif in amorphous Cu–Zr alloys, which is why we have focused the characterization of topological short range order on the population of Cu-centered FIs.

In addition to the information on TSRO, the Voronoi analysis yields a Voronoi volume for each atom. Given the theory by Turnbull and Cohen [18], who defined the excess volume as the difference between the specific volume (analogous to the Voronoi volume) and the molecule volume (here: atomic volume) and assuming a constant atomic volume, an increase in Voronoi volume can be directly translated into an increase in excess volume.

For a comparative study of structural recovery inside the shear band and in the matrix, we have analyzed the average Voronoi volumes, the fraction of Cu-centered FIs, and the CSRO for a test volume of 2 nm thickness in the center of the shear band, as well as for a test volume in the matrix. In addition, we have scanned the average volumes and FI-fraction perpendicular to the SB-slip direction, to gain more insight in the local structural rearrangements during deformation and thermal treatment. Each scan shown in Figures **??** and 47 is an average of three single scans at different snapshots within a time interval of 300 ps, in order to minimize statistical fluctuations.

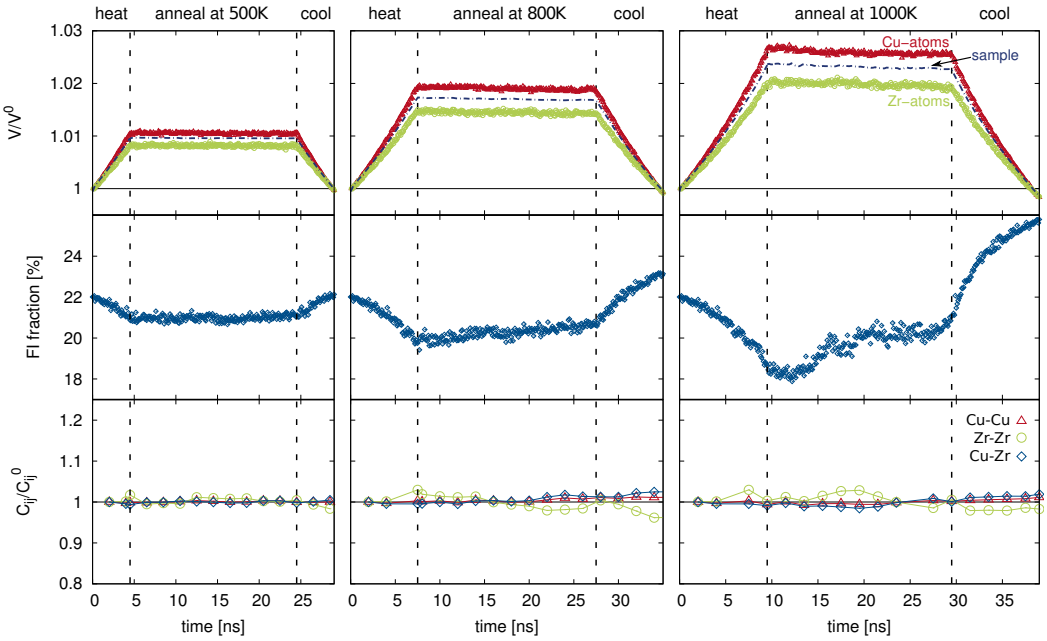

Figure 43: Annealing of the as-quenched $Cu_{64}Zr_{36}$ glass: Changes in relative volume, FI-fraction, and chemical short range order are shown for annealing temperatures of 500 K ($\approx 0.55T_g$), 800 K ($\approx 0.85T_g$) and 1000 K ($\approx 1.05T_g$). At 500 K, thermal activation is not sufficient to activate structural relaxations, while we observe a marginal release of free volume and increase in FI-fraction at 800 K. When the annealing temperature is above T_g, the glass structure relaxes substantially. The CSRO does not change significantly, independent of the temperature.

8.2 STRUCTURAL RELAXATION OF UNDEFORMED $CU_{64}ZR_{36}$ GLASS

The main goal of this study is to gain a better understanding of the structural relaxation of plastically deformed metallic glasses. Yet, even an as-prepared metallic glass is thermodynamically unstable and thermally activated atomic rearrangements lead to an increase in the overall configurational order of the system, namely an increase in packing density and an increase in chemical and topological short range order. Consequently, if we want to distinguish between the relaxation processes always occurring in a glass which was obtained by rapid quenching and the recovery of defects caused by plastic deformation, we first have to analyze an as-quenched (=virgin) metallic glass under annealing conditions.

Figure 43 shows the evolution of the Voronoi volume of Cu- and Zr-atoms relative to the initial volume, the content of Cu-centered full icosahedra (middle panels) and the CSRO (bottom panels), during annealing at 500 K, 800 K, and 1000 K. Before comparing the results for different annealing temperatures, we

want to point out two general features that are present in all three cases: (i) When comparing the relative Voronoi volumes of Cu- and Zr-atoms during heating, the larger thermal expansion for Cu-atoms stands out. The volume coefficients of thermal expansion below T_g can be estimated by

$$\alpha_v = \frac{\Delta V}{V_0 \cdot \Delta T} = \frac{V(500\text{K}) - V(50\text{K})}{V(50\text{K}) \cdot 450\text{K}}, \tag{8.1}$$

using the sample volume at 50 K and 500 K, we get a value of $\alpha_v = 2.1 \cdot 10^{-5}$ K^{-1} for the whole sample. This value is in good agreement with experimental values of thermal expansions for other metallic glasses as reported in literature (*e.g.*, Ref. [142, 146]). The partial thermal expansion coefficients for Cu- and Zr-atoms are approximated by inserting the according average Voronoi volumes in equation (8.1). Using this approach we get values of $\alpha_v^{Cu} = 2.5 \cdot 10^{-5}$ K^{-1} and $\alpha_v^{Zr} = 1.9 \cdot 10^{-5}$ K^{-1}. One possible explanation for this difference in thermal expansion is a stronger anharmonicity in the interatomic potential for Cu-atoms as compared to Zr-atoms. In order to confirm this assumption we have simulated energy-volume-curves for Cu and Zr (see Fig. 44). We have, therefore, homogeneously strained the virgin glass sample to a fixed volume, let the atomic positions relax and determined the potential energy contribution of Cu-atoms and Zr-atoms. The resulting curves were fitted by the Birch-Murnaghan equation of state [147] and the pressure derivative of the isothermal bulk modulus B_T', which is a measure for the anharmonicity of the potential, was evaluated. From B_T' we can approximate the Grüneisen parameter $\gamma \approx \frac{1}{2}(B_T' - 1)$ [148], which is directly proportional to the thermal expansion, thus, a larger γ means higher thermal expansion. Because of the strong variation of the fit results with the fitting interval, we have calculated B_T' as a function of the fitting interval. Over the whole range of fitting intervals considered, we obtain a higher B_T' for Cu (≈ 3.35) than for Zr (≈ 2.9); the resulting Grüneisen parameters are $\gamma_{Cu} = 1.18$ and $\gamma_{Zr} = 0.95$. Consequently, the higher thermal expansion for Cu can be explained by the stronger anharmonicity of the interatomic potential for Cu-atoms.

(ii) When the sample is heated, the population of Cu-centered full icosahedra decreases (see Fig. 43, middle panels). This decrease is a result of the anisotropic thermal expansion of the $Cu_{64}Zr_{36}$-metallic glass studied here, which leads to an elastic distortion of the icosahedral clusters in the sample and, therefore, the analysis detects a lower fraction of FIs. This effect is fully reversible and does not influence the results.

Next we compare the relaxation of excess volume, topological and chemical SRO in the undeformed sample at different temperatures. When the undeformed sample is heated to 500 K, the thermal expansion is linear indicating that no excess volume is released during heating. During annealing at 500 K, changes in the Voronoi volumes (as well as the sample volume) are hardly detectable and the final volumes after quenching are almost identical as in the as-quenched case. So

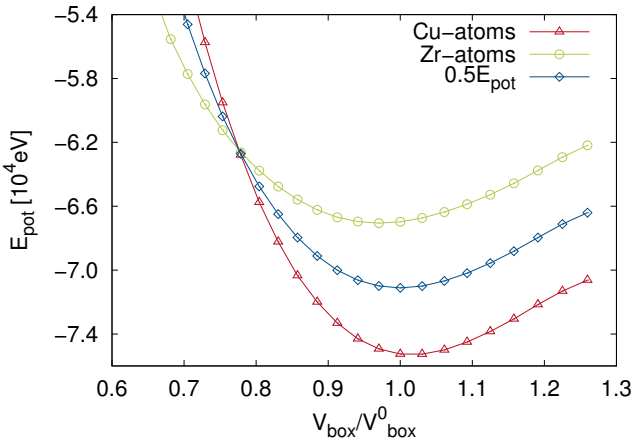

Figure 44: Energy-volume-curves for Cu-and Zr: a stronger anharmonicity in the interatomic potential for Cu-atoms as compared to Zr-atoms leads to a bigger thermal expansion for the Cu-atomic volumes.

on the time scales studied here, no excess volume is released at a temperature of 500 K. This is in good agreement with the behavior of the TSRO: taking statistical fluctuations into account, the FI-fraction in the virgin sample is almost the same as the FI-fraction after annealing at 500 K and subsequent quenching. The same holds true for the chemical short range order, where the changes during annealing are of the order of statistical fluctuations. During annealing at 800 K, we observe a marginal volume decrease and the final sample volume is 0.04% smaller as compared to the virgin sample. Again, we find the excess volume to be linked to the FI-fraction, which increases by approximately 1% during annealing at 800 K. As for an annealing temperature of 500 K, changes in the CSRO are of the order of statistical fluctuations and no significant trend is detected. The thermal expansion deviates from a linear behavior when the glass transition temperature is passed during heating to 1000 K. After annealing at $T > T_g$, a total amount of 0.14% free volume (with respect to the sample volume) has been released and, at the same time, the FI-occupation is increased by 4%. Interestingly, the volume release as well as the increase in the FI-fraction only occur within the first 10 ns of annealing, before both saturate. A possible explanation is that in the final structure, 78% of all atoms are part of Cu-centered full icosahedra. Since dense packing is not possible using only FIs (due to its fivefold symmetry), packing frustration will occur at a certain FI-density, when a further increase in the number of FIs would lead to a volume increase. Again, the CSRO does not change significantly.

To summarize this section, we have found that the thermal expansion for Cu-atoms is larger than for Zr-atoms. At an annealing temperature of 500 K, almost

no structural relaxation occurred in the as-prepared $Cu_{64}Zr_{36}$ glass, while we observe an increase in the FI-fraction accompanied by a decrease in excess volume at 800 K and 1000 K. In agreement with our results on shear band formation above, changes in the TSRO are directly coupled to changes in the packing density. The CSRO is not changed by thermal annealing on the time scales studied here.

8.3 SHEAR BAND RECOVERY

After analyzing the structural relaxation of an as-prepared bulk sample under annealing conditions, this section will focus on the structural recovery of a deformed metallic glass. Figure 45 shows the evolution of the relative volumes of the sample and the Cu- and Zr-atoms (1st and 2nd row of panels), changes in the FI-fraction as an indicator for the TSRO (3rd and 4th row of panels), and the relative nearest neighbor correlation indices representing variations in the CSRO (5th row of panels), in shear band and matrix for annealing temperatures of 500 K, 800 K, and 1000 K. The relative volumes and correlation indices are given with respect to the according values for the undeformed sample. Looking at the variation in the relative volumes (Fig. 45, top panels) it is obvious that the structural recovery of the deformed glass is overlayed with the thermal expansion. The same holds for the recovery of the icosahedral short range order (Fig. 45, third row of panels), which is overlayed by the decreasing FI-fraction due to anisotropic thermal expansion. Consequently, in order to analyze shear band relaxation the data has to be deconvolved. In the case of the volume data, this is done adapting a model by Taub and Spaepen [146], according to which the equilibrium thermal expansion of a glass α_{th} consists of an isoconfigurational contribution resulting from the anharmonicity of the interatomic potential α_{iso} and a structural change term reflecting the changes in packing density and chemical order during heating α_{struc}:

$$\alpha_{th} = \alpha_{iso} + \alpha_{struc}. \tag{8.2}$$

Given the definition of the volume coefficient of themal expansion in equation (8.1), we can write:

$$\frac{\Delta V_{def}}{V^0_{def}} = \frac{\Delta V^{iso}_{def}}{V^0_{def}} + \frac{\Delta V^{struc}_{def}}{V^0_{def}}, \tag{8.3}$$

where ΔV_{def}, ΔV^{iso}_{def}, and ΔV^{struc}_{def} are the total volume change, the volume change due to isoconfigurational thermal expansion, and the volume change due to structural relaxation; V^0_{def} is the volume of the deformed sample before heating or quenching, respectively. Since we do not know the isoconfigurational contribution to thermal expansion of the deformed sample, we approximate this quantity by the thermal expansion of the undeformed sample assuming that structural

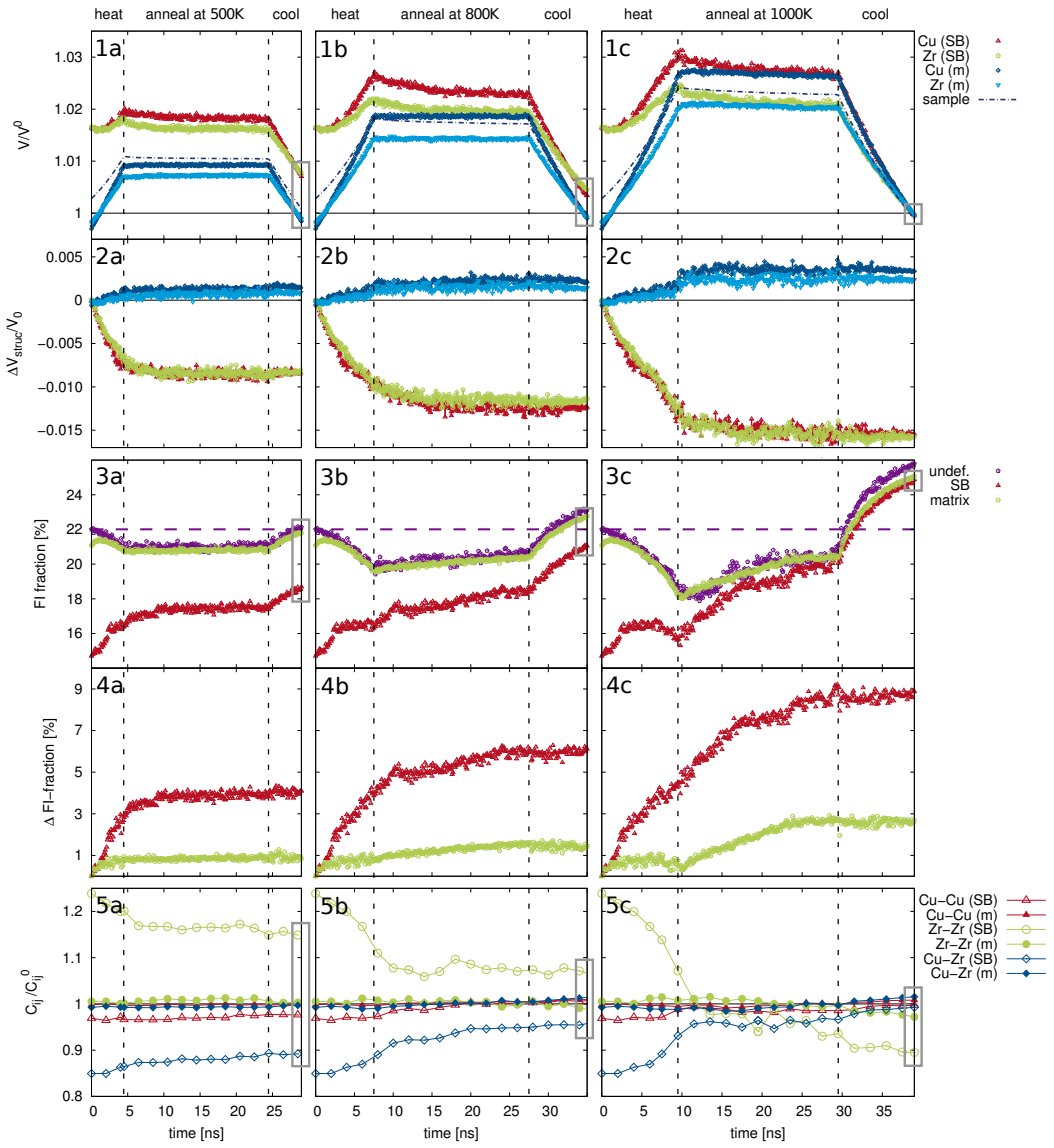

Figure 45: Annealing of a pre-deformed sample: Changes in relative volume (1a-c) and volume changes due to structural relaxation (2a-c), evolution of FI-fraction (3a-c) and increase in FI-fraction due to structural rearrangements (4a-c), and the recovery of the chemical short range order (5a-c) are shown for annealing temperatures of 500 K ($\approx 0.55T_g$), 800 K ($\approx 0.85T_g$) and 1000 K ($\approx 1.05T_g$). At 500 K, only the SB relaxes while the matrix remains unchanged; the thermal activation does not allow a full recovery. At 800 K, both, SB and matrix, undergo structural relaxation.

relaxations during heating of the virgin material are negligible on the time scales studied here. With this assumption and with $\Delta V = V(T) - V_0$, we can estimate the volume change resulting due to structural relaxation ΔV_{struc} by

$$\Delta V_{struc}(T) = V^0_{def}\left[\frac{V_{def}(T) - V^0_{def}}{V^0_{def}} - \frac{V_{undef}(T) - V^0_{undef}}{V^0_{undef}}\right]. \quad (8.4)$$

In order to separately study the relaxation of shear band and matrix, we have calculated the average Voronoi volumes in a test volume inside the shear band and in the matrix and compared them to the according average Voronoi volumes in the undeformed sample to evaluate equation (8.4). The resulting volumetric changes are identical to changes in excess volume due to the recovery of structural defects introduced by plastic deformation (see Fig. 45, 2nd row of panels).

In order to eliminate the effect of anisotropic thermal expansion from the evolution of the FI-occupation we again compare data for the deformed sample to data for the undeformed sample, using the following relation:

$$\Delta c^{FI}_{struc}(T) = c^{FI}_{def}(T) - \Delta c^{FI}_{undef}(T), \quad (8.5)$$

where Δc^{FI}_{struc} is the change in FI-fraction due to structural recovery, $c^{FI}_{def}(T)$ is the FI-fraction in the deformed sample at temperature T, and $\Delta c^{FI}_{undef}(T)$ is the corresponding change in FI-fraction during heating/quenching of the undeformed sample. Using this approach we obtain the absolute changes in FI-fraction during heating, annealing and quenching (see Fig. 45, 4th row of panels).

The results shown in Fig. 45 illustrate that the recovery of a deformed metallic glass involves the relaxation of excess volume, topological, and chemical short range order: Independent of the annealing temperature we observe a decrease in excess volume in the shear band, while the excess volume in the matrix increases (see 2nd row of panels). The reason for the volume increase in the matrix is that excess volume is transported from the SB into the surrounding material, which was subjected to a compressive strain during SB formation and, therefore, recovers by the absorption of excess volume. The fraction of Cu-centered FIs increases in the SB as well as in the matrix (see 4th row of panels) and the CSRO, which was only affected inside the SB, tends to go back to the initial state before deformation (see 5th row of panels). As mentioned in the previous sections, we find a strong connection between the local concentration of Cu-centered full icosahedral clusters and the packing density or excess volume, respectively. In order to further investigate the nature of this correlation, we have plotted the change in Voronoi volume due to structural relaxation over the according change in FI-fraction in the shear band during heating, annealing and quenching for different annealing temperatures. The resulting graph (see Fig. 46) reflects the aforementioned observations: we see a linear decrease in the Voronoi volumes, which is equivalent to a decrease in excess volume with increasing FI-fraction,

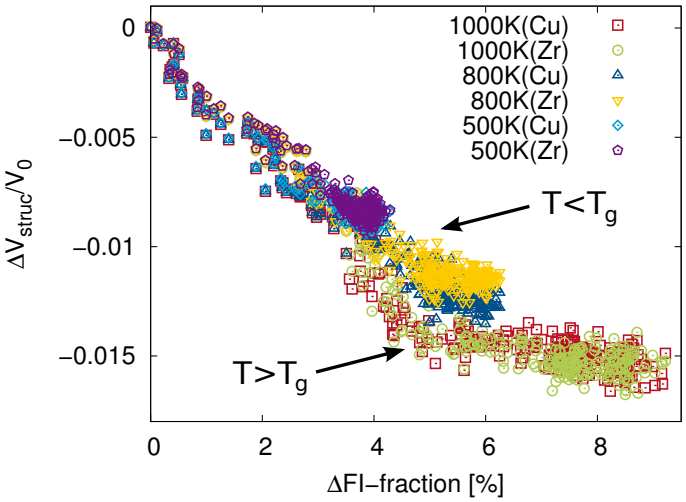

Figure 46: Correlation between recovery of icosahedral SRO and the release of free volume.

at least if the temperature is below T_g. For temperatures above T_g, the data points deviate from the linear correlation and we first observe a steeper slope due to faster relaxation of excess volume, followed by a regime where the Voronoi volumes hardly change despite a further increase in FI-fraction. This can again be explained by the packing frustration of icosahedral clusters as discussed in the previous section for the case of the undeformed sample. In fact, when comparing the final FI-fraction after annealing at 1000 K in SB and undeformed sample (see marked area in Fig. 45, panel 3c), we find the SB-value to be only slightly lower than the final FI-fraction in the undeformed sample.

The relaxation mechanisms are thermally activated and depending on the annealing temperature different degrees of recovery are achieved during the studied period of time (see also scans of the final samples after annealing in Fig. 47): After annealing at 500 K structural inhomogeneities are still present. The average Voronoi volume in the SB is still about 0.7% higher as compared to the undeformed material, while the volumes in the matrix are about 0.2% lower (see marked area in panel 1a). At the same time, the FI-fraction in the shear band is almost 4% lower than in the matrix (see marked area in panel 3a). The same trend is found in the CSRO, where considerable differences between SB and matrix are still present after annealing (see marked area in panel 5a). When the deformed sample is annealed at 800 K, which is still below the glass transition temperature, a higher degree of relaxation is obtained since the increased annealing temperature enables the activation of more relaxation mechanisms. Yet, we still observe a frozen amount of excess volume inside the SB (see marked area in panel 1b) and the TSRO and CSRO in the SB deviate from the matrix (see marked areas

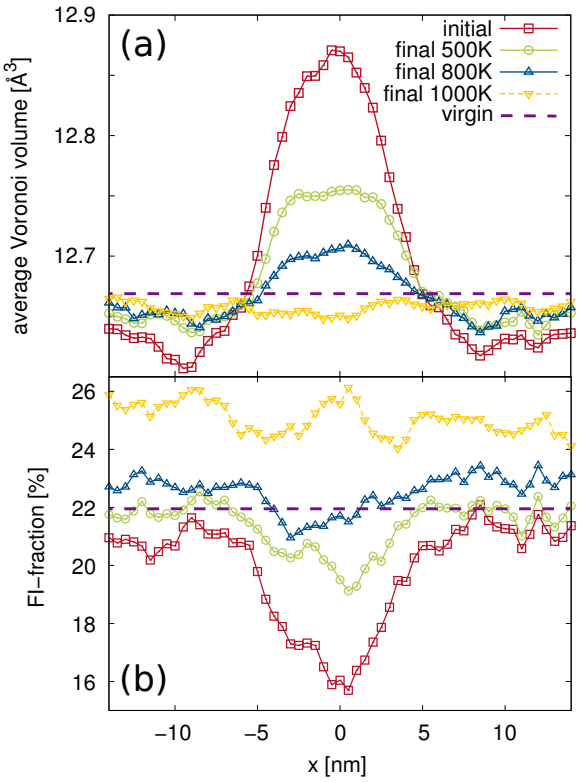

Figure 47: Linear scans of the deformed sample before (= initial) and after annealing (= final) at 500 K, 800 K and 1000 K showing (a) the change in average volume of Cu-atoms and (b) the recovery of Cu-centered full icosahedra.

in panel 3b and 5b). If the annealing temperature is above T_g (1000 K), the homogeneous microstructure is recovered and all defects introduced by plastic deformation are fully relaxed (see marked areas in panel 1c and 3c). At the glass transition, thermal activation is sufficient to activate all mechanisms contributing to structural recovery and, therefore, also structural defects present in the as-prepared glass can be relaxed during annealing, as observed in the case of the undeformed sample (see previous section). And in fact, the final FI-fraction after annealing (marked area in panel 3c) is about 3% higher than in the as-prepared material (dashed line in panel 3c), both in SB and matrix.

Major structural relaxations already occur inside the shear band during heating. The release of excess volume, the FI-fraction and the NN-correlation indices saturate after a certain annealing time (see rows two, four, and five in Fig. 45). This initial ultra-fast recovery is not observable with experimental techniques and will most likely already occur during deformation at experimental deformation rates.

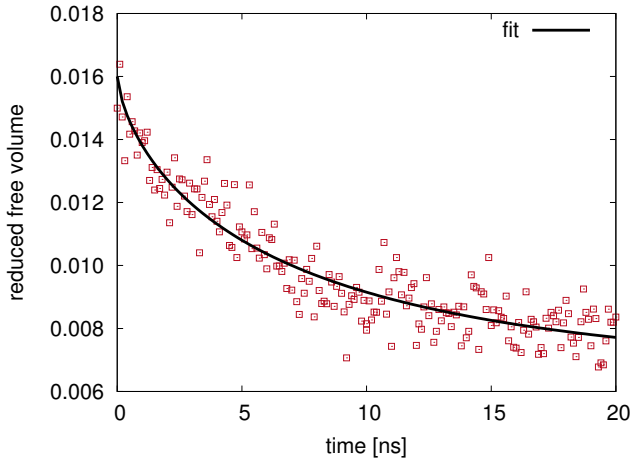

Figure 48: Isothermal change in free volume during annealing at 800 K. The data was fitted by a stretched exponential function ($\Delta\beta = 4\%$; $\Delta\tau = 3\%$).

In order to extract quantitative information on the relaxation kinetics we have, therefore, only considered the isothermal part of the volume relaxation. According to Haruyama and Inoue [149], the change in reduced free volume x during isothermal annealing at a temperature below T_g can be fitted by a stretched exponential function

$$x \quad = \quad x_{eq} + (x_0 - x_{eq}) \cdot \exp\left[-\left(\frac{t}{\tau}\right)^{\beta}\right], \tag{8.6}$$

where x_{eq} is an equilibrium value of the reduced free volume at $t \longrightarrow \infty$, x_0 is the initial value, τ is the relaxation time, and β is the Kohlrausch exponent. We have fitted equation 8.6 to the volume relaxation data obtained during annealing of the virgin sample and the shear band in the deformed sample (only for annealing temperatures below T_g). The reduced free volume can be estimated by comparing the density of the glass to the density of an ideal glass (for details see Ref. [149]). Due to the lack of data for an ideal glass we have used the value of the undeformed glass after annealing at 1000 K, which we assume to be close enough to the state of a relaxed glass. Since the number density is equal to the reciprocal average Voronoi volume, we have calculated the reduced free volume by $x = (\overline{V} - \overline{V}_{ideal})/(0.5 \cdot \overline{V}_{ideal})$, where $\overline{V}$ is the average Voronoi volume in the annealed sample and $\overline{V}_{ideal}$ is the average Voronoi volume in the relaxed glass at the corresponding temperature. Numerical fits to our data (see Fig. 48 as an example) yield a Kohlrausch exponent $\beta = 0.63$, which is in the range of what has been reported in literature for the isothermal relaxation of metallic glasses below T_g (*e.g.*, Ref. [149]). The Kohlrausch exponent takes values between 0 and

1, where $\beta = 1$ reflects a single activation energy [16], while a smaller value suggests a broad distribution of activation energies. The structural relaxation observed in our simulations is, therefore, facilitated by a number of processes with different activation barriers. Interestingly, we find the same β for shear band and undeformed sample, which indicates that the same processes that occur during the relaxation of an as-prepared metallic glass are involved in the recovery of the highly strained material inside the shear band. The difference, however, is found in the relaxation times, which is 13-times longer in the virgin material as compared to the SB for annealing at 500 K, or 7-times longer for an annealing temperature of 800 K, respectively.

In this section we have studied the structural recovery of a pre-deformed $Cu_{64}Zr_{36}$ glass during thermal annealing at different temperatures below and above T_g. To characterize the relaxation mechanisms we had to eliminate the effect of thermal expansion from our data by comparing the data for the pre-deformed sample to the data for an undeformed sample. We found the relaxation of excess volume as well as the recovery of chemical and topological short range order to contribute to structural recovery. A linear correlation between the increase in packing density with the increase in icosahedral short range order was found for annealing temperatures below T_g. The recovery mechanisms are thermally activated and the degree of recovery depends on the annealing temperature: after annealing at 500 and 800 K, structural inhomogeneities were still significant, whereas annealing at a temperature above T_g leads to a homogeneous microstructure with lower excess volume and a higher degree of topological short range order as compared to the virgin sample.

8.4 ATOMIC SCALE RELAXATION MECHANISMS

In order to identify the mechanisms contributing to structural relaxation in shear band and matrix at different temperatures, we have utilized the ability of MD simulations to study individual atomic jump processes. Since relaxation mechanisms in the supercooled liquid regime differ from mechanisms in the glassy state and studying individual jumps becomes more difficult due to high atomic mobilities, we have limited the characterization of relaxation mechanisms to temperatures below T_g. During a time interval of 20 ns at constant temperature, the jump lengths inside SB and matrix were evaluated for both atomic species and the resulting distributions were plotted in Fig. 49. Again, we have performed the same analysis for the undeformed sample for comparison. At an annealing temperature of 500 K the jump length distributions for the undeformed sample, as well as for SB and matrix in the pre-deformed sample contain only one peak. This peak originates from displacements much shorter than the nearest neighbor (NN) distance ($\approx$2.6Åfor Cu–Cu–neighbors) and is, therefore, referred to as original site peak (OSP). This observation is typical for metallic glasses and hints to a

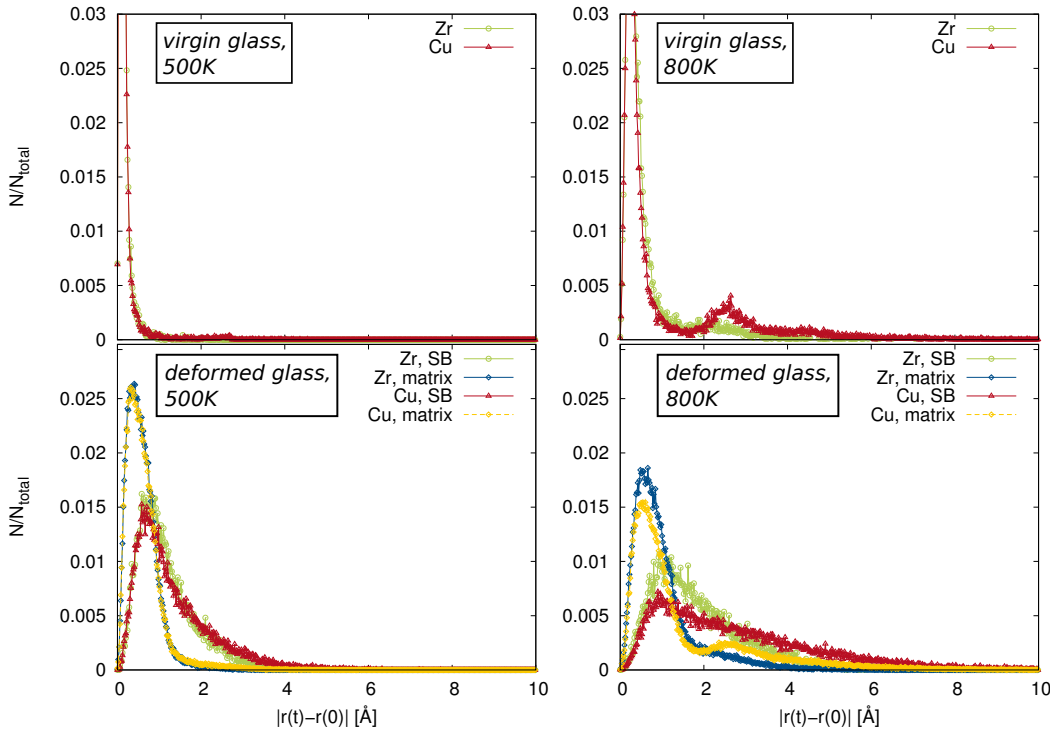

Figure 49: Jump length distribution for undeformed and deformed samples after $\Delta t =$ 20ns during annealing at different temperatures.

collective diffusion mechanism where groups of atoms jump in concert. Due to the lacking particular length scale for displacements in the glassy state, atomic jumps lead to a Gaussian-like broadening of the OSP with time, while different atomic mobilities, i.e., dynamic heterogeneities, are reflected in a deviation from Gaussianity and tails to longer distances [150, 151]. The OSP for the matrix of the deformed sample is broadened as compared to the virgin sample and shifted to larger displacements, which indicates a higher mean square displacement (MSD) and, thus, higher diffusivity. In the case of the shear band, the peak is located at even higher displacements and the peak broadening is significantly stronger as compared to the matrix with a pronounced tail to larger jump lengths. This is in good agreement with the above findings of an increased excess volume in the heavily deformed material in the shear band. Interestingly, the distributions for Cu and Zr atoms are almost identical for shear band and matrix, as well as for the virgin material, despite the significant size difference and, therefore, supposedly increased mobility of Cu atoms. This, however, is a typical feature of a collective jump process which is hardly influenced by individual atomic mobilities [150].

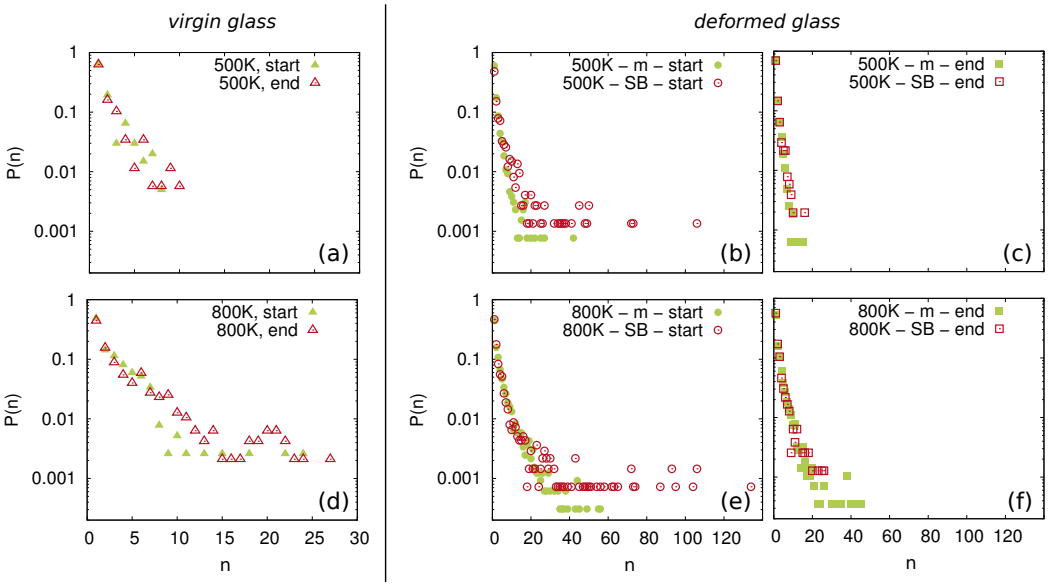

Figure 50: Probability distribution $P(n)$ of chain length n (=number of atoms involved in a collective jump event) during annealing at 500 K (a-c) and 800 K (d-f) for undeformed and deformed $Cu_{64}Zr_{36}$ glass. For the deformed samples we have analyzed $P(n)$ at the beginning of isothermal annealing (= start) and after 20 ns (= end); the evaluated time interval was 200 ps in all cases.

Next, we have characterized collective jumps in SB and matrix qualitatively as well as quantitatively, to confirm the assumption of collective motion as the dominant relaxation mechanism at 500 K. For detecting individual jump events we neglect atoms with a displacement below 1 Å; the remaining atoms are divided into clusters by analyzing the nearest neighbor environment: if two atoms are nearest neighbors and have both jumped within a time interval of 200 ps, they are assumed to belong to the same jump event. For a quantitative analysis of the collective jump process we have plotted the probability distribution $P(n)$ of the chain length n for different test volumes in the deformed and undeformed sample at the beginning of isothermal annealing and after 20 ns (Fig. 50); for better statistics, we have averaged over three individual distributions. At the beginning of annealing at 500 K, collective jumps inside the SB involve up to 106 atoms and the average chain length is considerably higher than in the matrix (Fig. 50 (b)), where the maximum chain length is only 42 atoms. After 20 ns at 500 K (Fig. 50 (c)), the maximum chain length in both SB and matrix is decreased to 15 atoms, which is close to the value we observe for the virgin sample (Fig. 50 (a)). This is in good agreement with the spatial distribution of atomic jumps given in Fig. 51, where at the beginning of annealing (= start) we observe a considerably higher frequency of atomic jumps in the SB as compared to the matrix, while after 20 ns

at 500 K, the distribution of diffusive jumps is homogeneously distributed in the whole sample and the overall frequency of jumps is smaller than at the beginning of annealing. When analyzing individual collective jumps at the beginning of annealing, as displayed in Fig. 52, we find that at 500 K most atoms jump in a chain-type process in the matrix as well as in the SB. While the chains in the matrix are mostly linear, the collective jumps in the SB are mostly longer, more complex chains containing several branches.

During annealing at 800 K, an additional process contributes to structural relaxation: The jump length distributions for Cu-atoms (see Fig. 49 (c) and (d)) contains an additional feature besides the OSP at about 2.6Å, which is equal to the Cu-Cu-nearest neighbor distance. In the case of the virgin sample and the matrix of the deformed sample, the additional peak is clearly resolvable; in the SB, however, the OSP-broadening is so strong that the NN-peak is only visible as a hump in the distribution. Due to the elevated temperature, Cu-atoms are able to perform nearest neighbor jumps in addition to their contribution to collective motion. The bigger Zr-atoms are less mobile and the frequency of Zr-nearest-neighbor-jumps is not significant and, therefore, no additional peak appears in in the Zr-distribution. The broad distribution of jump lengths in the SB with a long range tail up to several NN-distances can be explained by secondary jumps during the studied time interval of 20 ns. Comparing the chain length distributions for 500 K (Fig. 50 (a-c)) and 800 K (Fig. 50 (d-f)), we find a higher number of atoms per collective jump at an annealing temperature of 800 K, in SB and matrix, as well as in the undeformed sample. This is in good agreement with what is known about collective motion in metallic glasses, where an increase in temperature results in longer chains and larger individual displacements [152]. Again, the number of atoms involved in one individual jump process is considerably higher at the beginning of isothermal annealing (Fig. 50 (e)) than after 20 ns(Fig. 50 (f)). The nature of individual collective jumps at the beginning of annealing at 800 K (see Fig. 52) is also chain-like. In the matrix, the atomic chains are still mostly linear, but branched chains are found more frequently than at 500 K. Apart from a number of chains with less than 10 atoms, which are mostly linear, collective jumps in the SB at 800 K are complex networks of branched chains involving a large number of atoms. These clusters of jumping atoms are evocative of a flow-like motion, as typically found in the undercooled melt (*e.g.*, Ref. [153]). The spatial distribution of diffusional jumps in the deformed sample (see Fig. 51 (right)) shows that at 800 K structural rearrangements occur in the whole sample and are not limited to the SB, as observed during annealing at 500 K. This is in line with the findings above, where we hardly observed structural relaxations in the matrix at 500 K in contrast to a significant recovery of short range order at 800 K. Another characteristic of the relaxation mechanism becomes obvious when taking a closer look at the distribution of atomic displacements during the total annealing time of 20 ns (see Fig. 51 (bottom)): the diffusive jumps are not homogeneously distributed, but the images suggest that mobile atoms

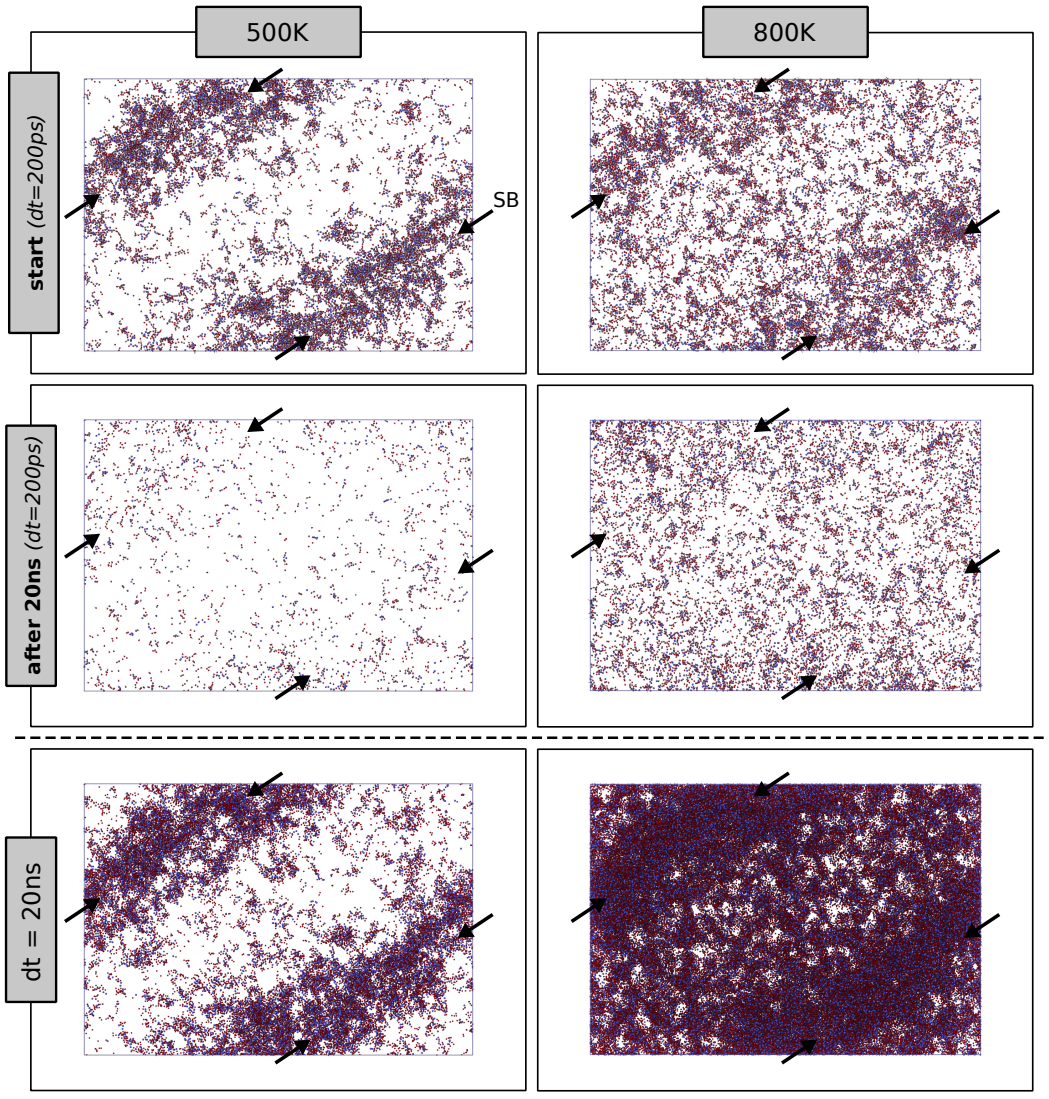

Figure 51: Atomic displacements in the whole sample during recovery annealing at 500 K and 800 K at the beginning of isothermal annealing (= start, top row), after 20 ns annealing (middle row), and for the total annealing time of 20 ns (bottom row). The arrows mark the position of the shear band. Only atoms with atomic displacements larger than 1.0Å for annealing at 500 K and 1.2Å for annealing at 800 K are displayed; red atoms are Cu, blue atoms Zr.

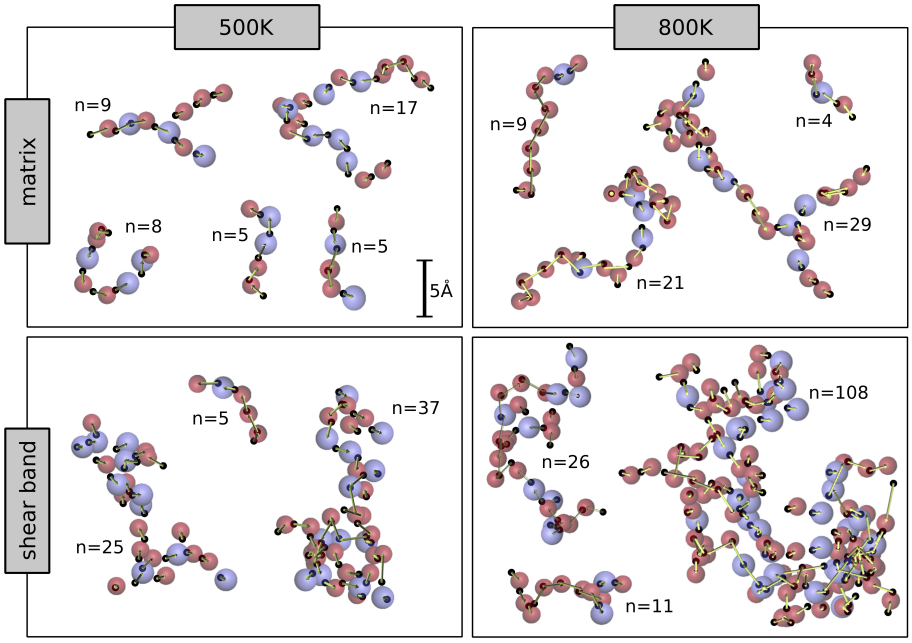

Figure 52: Collective jumps in shear band and matrix at the beginning of annealing at 500 K and 800 K during a time interval of 200 ps. Red and blue spheres represent Cu- and Zr-atoms at $t = 200$ ps, while the black dots represent the initial positions at $t = 0$; the arrows represent the atomic displacement vectors.

have jumped in chains between a network of immobile atoms. This interpretation would fit to the observed non-Gaussianity in the jump length distribution (Fig. 49), which, as mentioned before, is related to a dynamic heterogeneity of the relaxation mechanism.

The characterization of individual atomic jumps has shed light on the atomistic mechanisms carrying structural relaxations in pre-deformed metallic glass: At an annealing temperature of 500 K, structural relaxations occur solely by collective jumps in a chain-type process, while at 800 K, two processes contribute to structural relaxation, namely nearest-neighbor jumps of the small Cu-atoms in addition to collective motion. The individual atomic displacements as well as the number of atoms involved in one collective jump were higher for 800 K as compared to 500 K, and the chains often contained branches at elevated annealing temperature. At the beginning of isothermal annealing we found enhanced atomic rearrangements in the shear band at both temperatures, which occurred by cooperative jumps of a large number of atoms in complex clusters instead of linear chains, similar to flow-like motion in supercooled liquids. After 20 ns of

relaxation, atomic rearrangements occurred in the whole sample with the same frequency and the chain length distribution for SB and matrix was similar.

These results are also relevant for understanding the precipitation of crystalline phases in shear bands. Experimental studies revealed that during deformation at low homologous temperatures, nanocrystallites preferentially form inside shear bands [154, 155]. This observation was explained by increased atomic mobilities in SBs as a consequence of flow dilatation, which was supported by experiments on glassy polymers where increased mobilities inside SBs were measured directly [156]. On first glance, this appears contradictory to the current study, where enhanced atomic mobilities inside SBs were only detected within the first few nanoseconds of thermal annealing, time scales not sufficient for crystal formation. If crystallization or diffusion is, however, studied *in situ* during deformation, where the generation and annihilation of excess volume occur simultaneously, we expect increased diffusivities along SBs as long as a sample is strained. For the case of a pre-deformed sample subjected to thermal annealing, on the other hand, our results predict no enhanced diffusivity in the SBs. Instead, we assume that enhanced nucleation kinetics are a result of decreased nucleation barriers for crystalline phases in a SB due to defects in the short and medium range order.

8.5 SUMMARY

In summary, we have studied structural changes in a $Cu_{64}Zr_{36}$ glass during plastic deformation and thermal annealing at different temperatures above and below T_g. Considering the results presented in Chapter 7, it is not surprising that structural recovery during thermal annealing involves the relaxation of excess volume, topological and chemical short range order. The release of excess volume and the recovery of icosahedral short range order are linearly coupled for temperatures below T_g. If a critical FI-fraction is reached, however, the excess volume remains constant due to packing frustration. Depending on the temperature, different degrees of recovery were achieved during 20 ns of isothermal annealing: a full recovery of the SB was only observed for an annealing temperature above T_g, while after annealing at 500 K and 800 K substantial structural inhomogeneities remained. A detailed analysis of the atomistic mechanisms contributing to structural relaxation revealed that at 500 K collective motion is the only relevant relaxation mechanism, other than at 800 K, where Cu-nearest-neighbor jumps occur in addition to cooperative atomic jumps. The number of atoms per jump and the individual atomic displacements are higher at 800 K than at 500 K. The collective jumps showed characteristics of a chain-type process with mostly linear chains. At the beginning of isothermal annealing, however, we found jumps involving a large number of atoms in complex clusters or highly branched chains in the SB, similar to flow-like motion in supercooled liquids. Moreover, we found

a larger thermal expansion for Cu-atoms as compared to Zr-atoms caused by the stronger anharmonicity in the interatomic potential for Cu.

Coming back to the introductory remark on the discrepancy between free volume theory and experimental observations: Our results provide a link between free volume theory, which predicts instantaneous recovery of shear bands at elevated temperatures due to locally increased atomic mobilities like in the supercooled liquid, and experiments, where shear bands recover on time scales in the range of hours. At the beginning of annealing, we observe relaxation mechanisms in the shear band as typically found in the supercooled liquid state. Yet, due to the fast annihilation of excess volume in this regime, the atomic mobilities in the shear band decrease rapidly and after 20 ns annealing no enhanced diffusivity is found in the shear band anymore. A full recovery on short time scales is, therefore, inhibited.

Part V

NANOGLASSES

After studying the deformation behavior of defect-free, homogeneous metallic glasses in the previous parts, the following part deals with the influence of structural inhomogeneities, namely internal interfaces. Starting with one single interface in $Cu_{64}Zr_{36}$ glass generated by joining two planar surfaces, we study the structure, stability and properties of glass-glass interfaces. Due to their defective short range order and excess free volume of about 1-2 %, the interfaces exhibit similarities to shear bands that occur in deformed metallic glasses. When deformed in uniaxial tension, interfaces promote shear band formation and yielding occurs at lower stress than in a homogeneous bulk glass sample. This observation is the basis for the study presented in the subsequent chapter, where we characterize the mechanical properties of $Cu_{64}Zr_{36}$-nanoglasses, which are produced by the compaction of glassy nano-particles and, hence, contain a network of internal interfaces.

9

STRUCTURE, STABILITY AND MECHANICAL PROPERTIES OF INTERNAL INTERFACES IN $CU_{64}ZR_{36}$-NANOGLASSES

For crystalline materials it is a well established concept to tune materials properties by varying the grain size. Cold compaction of nanocrystallites as shown in Fig. 53 (top) leads to microstructures where a substantial fraction of the atoms are located in grain boundaries [157], which strongly influences the mechanical properties of a material. In general, grain boundaries are defined as 2-dimensional planar defects in crystalline materials separating domains of different crystallographic orientation but similar crystal structure [158]. The mismatch between adjacent grains is accommodated in the interface and, therefore, grain boundaries are typically less ordered regions. For the case of glasses, in contrast, there is no established concept of grain boundaries, due to the lack of translational symmetry and long-range order. If one considers, however, that a high degree of short and medium range order is found in glassy materials [28, 35], as well, the definition of a grain boundary in a glass as an internal interface enclosing a domain of atoms becomes conceivable. In bulk metallic glasses it is a well proven fact that planar defects do exist, namely in form of shear bands induced by plastic deformation (see Fig. 53 (bottom)). These shear bands exhibit an enhanced free volume and a modified local order [136, 59]. The question is whether planar defects in metallic glasses can be introduced by other means than deformation. Experimentally, indications for the existence of interfacial areas have been found in compacted nanopowders consisting of metallic glass-droplets [96], which were proposed to form a so-called nanoglass [159] (Fig. 53 (middle)). A theoretical analysis of the structure of interfaces in metallic glasses is, however, still lacking and recently published simulation results [160] suggest that, depending on the mechanical properties of the metallic glass, diluted interfaces relax instantaneously by plastic flow due to internal strains induced by the excess interfacial free volume.

Here, we report results of molecular dynamics simulations which provide direct evidence for the existence of internal interfaces in metallic glasses. We find that interfaces are characterized by an excess free volume as well as a defective short range order, similar to the structural features observed in shear bands. Under deformation, glass-glass interfaces act as precursors for shear band formation. Consequently, metallic glass containing internal interfaces (= nanoglass) will

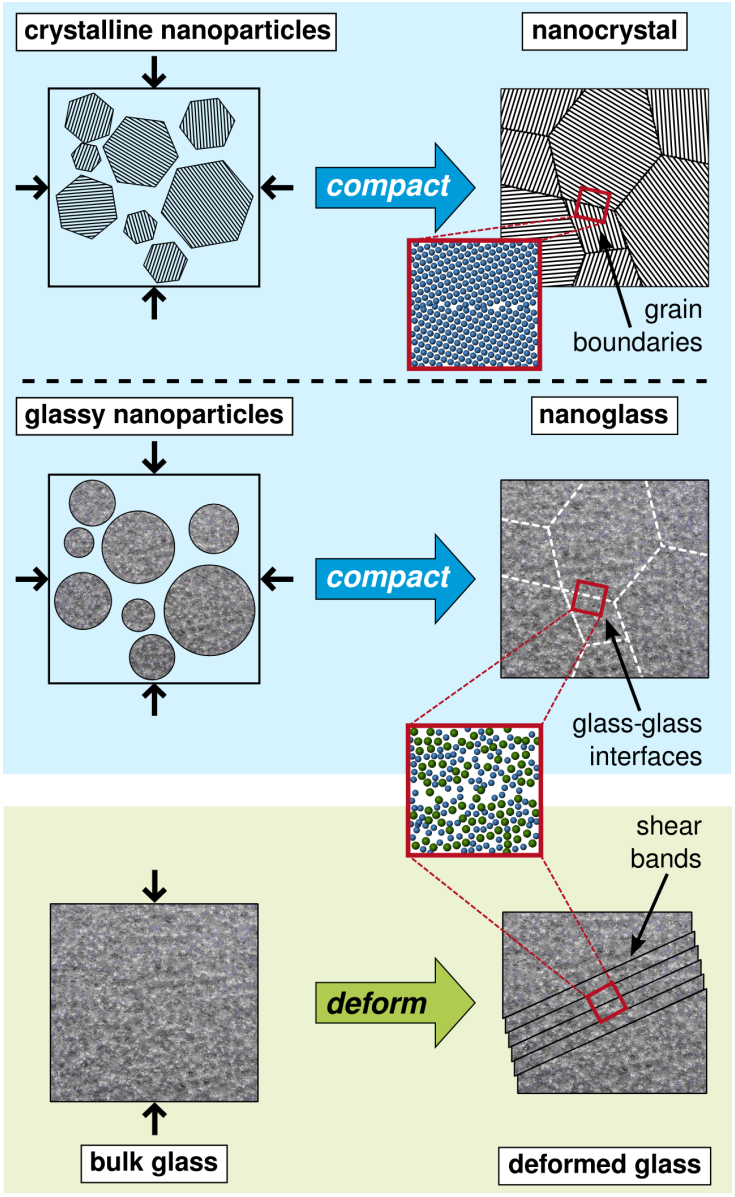

Figure 53: Different ways for tuning the structure of metallic glasses: Nanoglasses containing grain-boundary-like interfaces can be obtained by powder consolidation (middle), similar to the synthesis of nanocrystalline materials (top). Another approach to modify the glass structure is to introduce shear bands by pre-plastic deformation (bottom). Both, shear bands and interfaces are planar defects with modified topology.

show enhanced plasticity, similar to pre-deformed BMGs [80, 81, 82, 83, 84, 85]. Our results suggest that micro-structural features allow to tune mechanical (but probably also functional) properties of metallic glasses.

9.1 SIMULATION DETAILS

For studying the structure, stability and properties of internal interfaces in metallic glasses, we have performed classical molecular dynamics simulations [100] using the embedded-atom method potential for Cu–Zr by Mendelev et al. [105]; in all simulations an integration time step of 2 fs was used. An amorphous $Cu_{64}Zr_{36}$-sample was prepared by cooling from the melt: after relaxation at 2000 K for 2 ns to ensure chemical homogeneity, the melt was quenched to 50 K using a cooling rate of 0.01 K/ps. The atomic structure of the synthesized $Cu_{64}Zr_{36}$ glass exhibited good agreement with data reported in literature [43]. A planar glass-glass interface was prepared by joining two planar relaxed glass surfaces at low temperature (50 K). The sample geometry (4x8x12 nm^3; 22,836 atoms) is similar to a bicrystal-setup with 3dim. periodic boundary conditions containing one interface parallel to the yz-plane.

In order to characterize the mechanical properties of glass-glass interfaces, we have simulated the tensile deformation of a sample (36x8x58 nm^3; 949,135 atoms) containing one planar grain boundary, which was oriented in a 45°-angle to the tensile axis (z-direction) and the x-direction, to ensure maximum shear stress along the interface plane. For comparison we have also deformed a homogeneous bulk sample (36x8x75 nm^3; 1,296,000 atoms). Both samples are slab geometries with open boundaries in x- and periodic boundaries in y- and z-direction. The samples were deformed by applying a constant strain rate in z-direction of $4 \cdot 10^7\ s^{-1}$ at a constant temperature of 50 K. The pressure in y-direction was controlled to be 0 kbar, to allow for lateral contraction.

9.2 STRUCTURAL CHARACTERIZATION OF A GLASS-GLASS INTERFACE

Figure 54 (a) shows the distribution of Voronoi volumes and the fraction of Cu-centered full icosahedra in a $Cu_{64}Zr_{36}$ glass sample with one planar interface located at $x = 0$. In a region of about 1 nm width, the Voronoi volumes are increased by about 1-2 % with respect to the average bulk Voronoi volume Ω_0. Given the free volume expression by Turnbull and Cohen [18], who defined the free volume as the difference between the specific volume (analogous to our Voronoi volume) and the molecule volume (here: atomic volume) and assuming a constant atomic volume, the increase in Voronoi volume can be directly translated into an increase in free volume. Hence, the interface between two glassy grains is characterized by an excess free volume of 1-2 % in our model system.

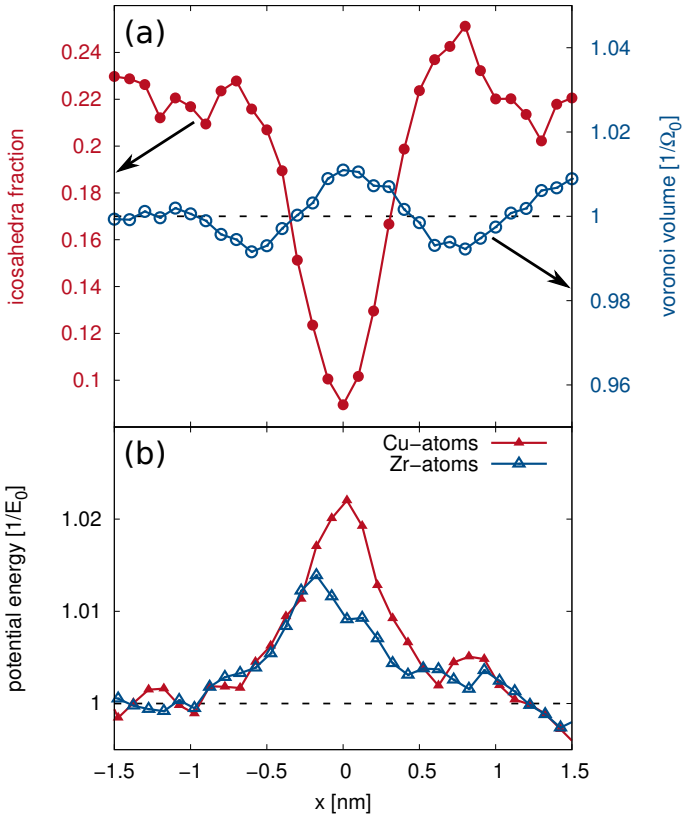

Figure 54: (a) Fraction of Cu-centered full icosahedra and Voronoi volumes and (b) potential energy as a function of the interface position $x = 0$.

But how is the localized free volume in the interface related to the atomic structure? For answering this question, we have evaluated the topology of the occurring Voronoi polyhedra, their frequency and spatial distribution, which gives a fingerprint of the atomic short range order. If we compare the interface, assuming a width of 1 nm, to the grain interior by analyzing the population of the most prominent Cu- and Zr-centered polyhedra (see Fig. 55; only VPs with a population >3% are shown), structural differences are obvious: In the case of the grain interior or bulk glass, respectively, the Cu-centered full icosahedron [0,0,12,0] is the most prominent VP with a population of about 22 % (with respect to the number of Cu-atoms in the system), which corresponds to a volume fraction of approximately 15 %. This Voronoi polyhedron is known to be a key structural motif in amorphous Cu–Zr–alloys, characterized by high packing density [45] and high shear resistance [43]. In the interface, this structural backbone [32] is defective, since the fraction of Cu-centered FIs is as low as 10 % (see Fig. 54(a), red data points), which yields an average FI-fraction in the interface of only 70 %

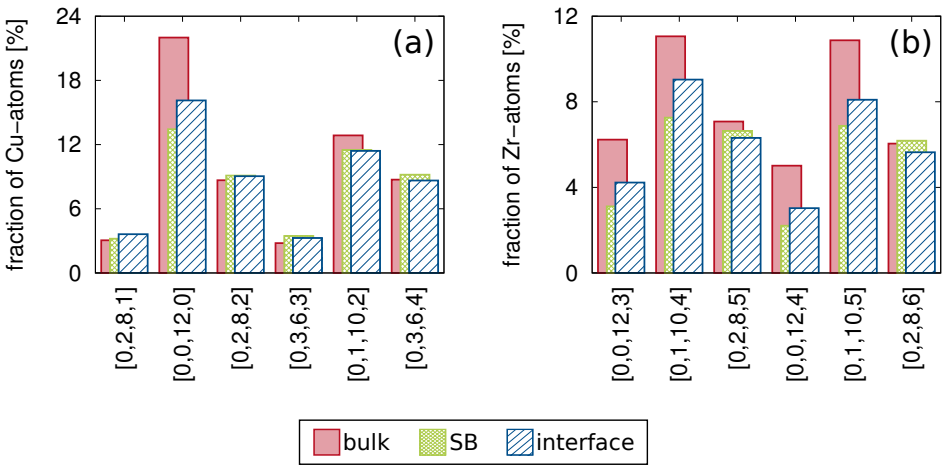

Figure 55: Population of (a) Cu-centered and (b) Zr-centered Voronoi polyhedra with a population >3%. In the grain interior ('*bulk*'), the Cu-centered full icosahedron is the most prominent VP. In the interface region ('*interface*'), which is assumed to be a volume of 1 nm width at the position of the initial sample surfaces, the FI-fraction is about 30 % lower. A similar deficiency is found for the Zr-centered polyhedra with indices [0,0,12,3], [0,1,10,4], [0,0,12,4], and [0,1,10,5]. The short range order of the interface shows similar features as found for a shear band ('*SB*') in the same glassy alloy.

of the bulk value. A similar deficiency in the interface is found for the Zr-centered polyhedra with indices [0,0,12,3], [0,1,10,4], [0,0,12,4], and [0,1,10,5]. Like the full icosahedron, these VPs are characterized by a large number of pentagonal facets, which are indicative for areas of dense atomic packing and, thus, high shear resistance [45]. The structural modifications inside the interface lead to an increase of the atomic potential energies (see Figure 54 (b)). By comparing a homogeneous $Cu_{64}Zr_{36}$ glass sample to a sample with an interface we estimate an interface energy of $0.9\,J/m^2$, which is in the range of grain boundary energies in polycrystalline materials (*e.g.* [161]). At this point, we can conclude that *interfaces between glassy grains in $Cu_{64}Zr_{36}$ are planar defects of about 1 nm thickness, with an excess free volume of approximately 1-2 % resulting from a defective short range order.* Similar features have been observed before in simulations of shear bands in metallic glasses [136, 59] and when comparing the Voronoi analysis of our interface to a shear band in the same glassy alloy, structural similarities are obvious.

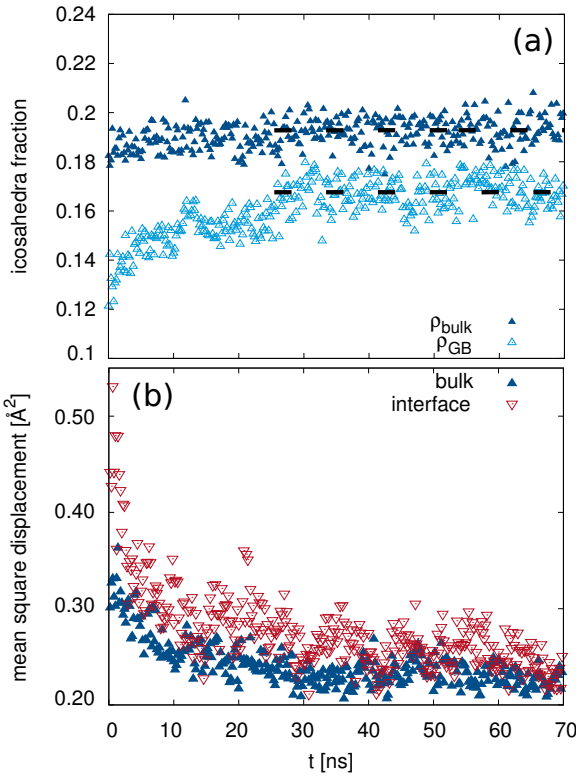

Figure 56: Recovery of (a) FI-short range order in interface (ρ_{GB}) and matrix (ρ_{bulk}), and (b) changes in the mean square displacements (evaluated for $\Delta t = 200$ ps) during annealing at 800 K.

9.3 STABILITY UNDER COMPRESSION AND THERMAL ANNEALING

The results discussed above demonstrate the possibility of interfaces between glassy grains, yet we have no evidence at this point that such defects in the glass structure will be stable. The examined interface has been produced at very low temperature (50 K) without applying any pressure, and, therefore, it is not quite clear how the interface structure might change at elevated temperatures or under pressure, on longer time-scales or if the model interface was generated in a different way. In order to address these points, we have studied the stability of a glass-glass interface under compression. This is particularly interesting with regard to cold compaction as a possible route for the synthesis of nanoglasses. During compression at a constant stress of 3 GPa, which is lower than the critical stress for shear band formation at 50 K, the population of Cu-centered full icosahedra has been evaluated. Most interestingly, we do not observe any topological changes induced by the applied stress, neither in the grain interior nor in the

interface. Hence, we conclude that a bulk glass produced by cold compaction of a glassy powder at can contain 2-dimensional defects between the consolidated glass particles. This result is in line with experiments, where evidence for interfaces was found in nanoglasses synthesized by powder consolidation [96].

Next, the long time stability of the glass-glass interfaces and their behavior at elevated temperature was studied. The sample with one planar boundary was annealed at a temperature of 800 K ($\approx 0.85 T_g$ of the dense glass) for 70 ns and, as an indicator for the degree of short range order, the population of Cu-centered full icosahedra in the interface region and in the grain interior was monitored (see Fig. 56). Within the first 25 ns of annealing, the fraction of full icosahedra increases in both test-volumes. The increase in the grain interior, however, is only in the range of 1 %-point and is attributed to the high cooling rates during preparation of the initial metallic glass. In the interface region, we see a stronger recovery. After 25 ns the FI-fraction saturates and for an extended simulation time of another 50 ns the population of full icosahedra remains constant, in the grain interior as well as in the interface (see linear fits in Fig.56) yielding a final difference between grain interior and interface of about 2 %–points. The recovery of icosahedral short range order coincides with changes in the mean square displacement calculated during annealing (Fig. 56(b)): At the beginning of isothermal annealing, the excess free volume in the interface and the high temperature enable high atomic mobilities leading to fast structural recovery. In this regime, structural relaxation is facilitated by collective atomic jumps and the number of jump events as well as the number of atoms contributing to one jump is higher in the interface as compared to the bulk material. The relaxation is associated with a release of free volume which, according to free volume theory (*e.g.*, [146]), causes a decrease in the atomic mobilities as seen in the rapid decrease in mean square displacement in the interface in Fig. 56(b). After 25 ns the atomic mobilities remain constant and the mean square displacement in the interface is only slightly higher than in the rest of the sample.

We do not observe a spontaneous relaxation of the interface and on MD time scales the glass structure does not recover. The high thermal stability of the interface is attributed to the atomic structure of the $Cu_{64}Zr_{36}$ glass studied here, which, as discussed in section 9.2, is characterized by a large population of VPs with high shear resistance. Consequently, the redistribution of excess free volume by homogeneous plastic flow is hindered, unlike in a previous study [160] where a softer metallic glass has been used with a flow strain of only 1% as compared to 4% for the $Cu_{64}Zr_{36}$ glass studied here.

Given the thermal stability on MD time scales, together with an interface energy which is comparable to grain boundary energies in polycrystalline metals and, therefore, a small driving force for structural recovery, we expect interfaces in metallic glasses to be stable at ambient conditions. This prediction is supported by very recent experimental results by Fang and co-workers [162], who found that a $Sc_{75}Fe_{25}$-nanoglass exhibits different deformation behavior than the corre-

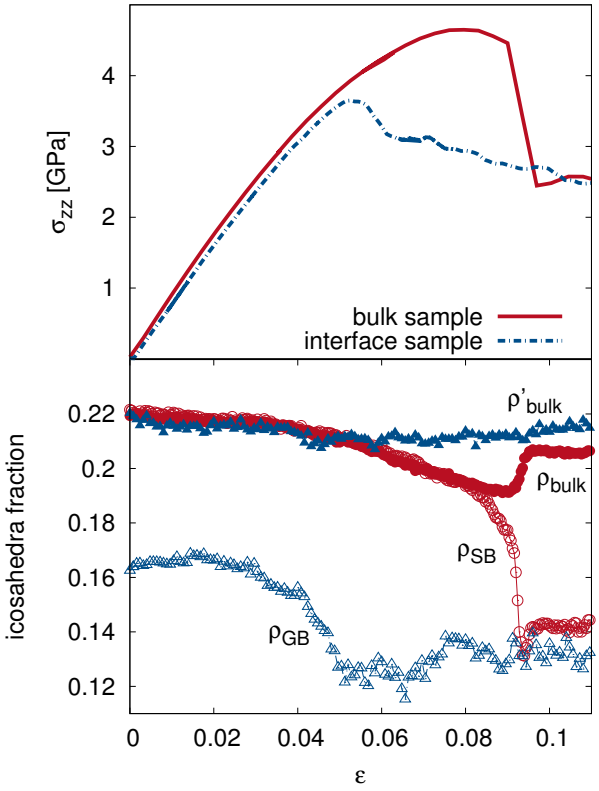

Figure 57: Stress-strain-curves for a sample containing one planar interface in 45° to the loading direction and a bulk glass sample under tensile deformation (top) and development of the FI-fraction during deformation in different sample regions (bottom). (ρ_{bulk}, ρ_{SB}: FI-fraction outside and inside the shear band region in the bulk glass sample; ρ'_{bulk}, ρ_{GB}: FI-fraction outside and inside the interface region in the interface sample.)

sponding melt-spun glass, even after annealing at 473 K. Moreover, shear bands in pre-deformed samples, which exhibit similar structural features as glass-glass interfaces, are also stable at ambient conditions and only recover at elevated temperatures on extended time scales [80, 81, 82, 83, 84].

9.4 DEFORMATION BEHAVIOR

In order to characterize the deformation behavior of a glass-glass interface, we have simulated the tensile deformation of a glass sample containing one interface, as well as the deformation of a homogeneous bulk glass for comparison. Compar-

ing the stress-strain curves for both samples (see Fig. 57), up to a strain of about 4 %, the interface-sample shows the same linear behavior as the homogeneous sample, only with a slightly reduced slope. This is a result of the lower fraction of full icosahedral clusters and, consequently, defective structural backbone in the grain boundary.

At strains higher than 4 %, yielding starts in both samples. For the bulk sample, this results in a bending of the stress-strain-curve accompanied by a decrease in the FI-fraction, homogeneously in the whole sample due to shear transformations. At a critical stress of 4.6 GPa, a SB nucleus is formed which subsequently propagates along a maximum stress plane, leading to a local drop in the FI-fraction. The stress decreases abruptly, when the shear band has penetrated the whole sample and SB slip occurs. Yet, if a sample initially contains a structurally softer region like an internal interface, where the activation barrier for shear transformations is lower due to the defective short range order and increased free volume, plastic deformation is expected to occur mainly in this region. And indeed, we observe strain localization in the interface-sample directly with the onset of plasticity. The FI-fraction in the grain boundary decreases from 16 % to approximately 14 % enabling shear-banding in the interface plane already at a stress of 3.6 GPa, which is 1 GPa less than for the bulk sample (see Fig. 57). The grain interiors, on the other hand, hardly contribute to plasticity at all, and the FI fraction remains almost constant during deformation. *Thus, an interface in a metallic glass can act as a shear band precursor,* promoting plastic deformation in the interface plane, which is in good agreement with the afore mentioned experimental results on a $Sc_{75}Fe_{25}$-nanoglass, where increased compressive plasticity due to the formation of multiple shear bands is observed [162]. Similarly, in pre-deformed metallic glasses pre-induced shear bands were found to act as softer phase with lower barriers for shear band nucleation [80, 81, 82, 83, 84].

The different degree of shear localization is reflected in the atomic level structure of the deformed samples (see Fig. 58). For the bulk sample as well as for the interface sample, the shear band is characterized by an excess free volume of about 1 % with respect to the average atomic volume in the undeformed bulk glass. The icosahedra fraction inside the shear bands is 14 %, again for both samples. The difference, however, between the two samples lies in the glass outside the shear band: while the atomic volumes and the icosahedra population in the whole bulk-sample differ from the undeformed values, even outside the shear band, the atomic level structure in the grain interiors of the interface-sample has hardly changed during deformation.

9.5 SUMMARY

In summary, we investigated the structure, stability and mechanical properties of internal interfaces in an amorphous $Cu_{64}Zr_{36}$-alloy by MD simulations. Our

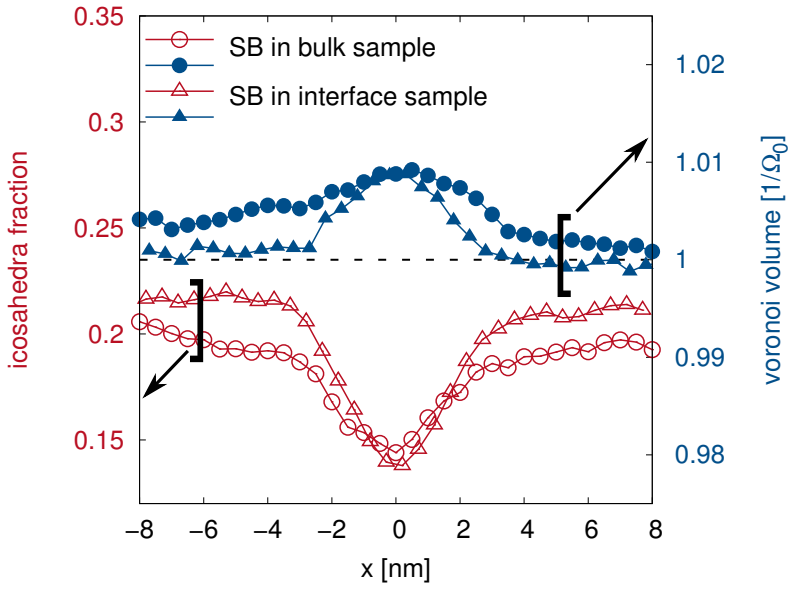

Figure 58: Atomic structure of deformed samples at 12 % tensile strain: linear scans of average Voronoi volume and FI-fraction reveal similar features for the SB along the interface compared to the SB in the bulk sample. The atomic structure in the surrounding matrix is hardly affected for the case of the SB formed in a pre-existing interface, while in the bulk sample the matrix structure is modified during deformation.

results provide evidence for the existence of glass-glass interfaces, which are characterized by a defective short range order and an excess free volume of about 1-2 %. These interfaces are stable on MD time scales and even after annealing at a temperature close to T_g the atomic structure of the interface clearly differs from the bulk glass. When deformed in uniaxial tension, the *softer* glass in the interface allows for shear band formation at lower stress compared to a bulk glass sample, similar to the shear bands in a pre-deformed metallic glass.

10

MECHANICAL PROPERTIES OF METALLIC NANOGLASSES

Given the results presented in the previous chapter, we expect samples synthesized by the consolidation of glassy particles, *i.e.* nanoglasses, to show significantly different mechanical properties than bulk metallic glasses produced by other techniques. By introducing shear band precursors like interfaces, shear localization can be controlled to achieve a more homogeneous plasticity, similar to the case of pre-deformed metallic glasses (see Section 1.3.2).

In this chapter, we investigate the mechanical properties of $Cu_{64}Zr_{36}$ nanoglasses under tensile load using MD simulations and compare to the case of a homogeneous bulk glass. Whereas the interfaces studied in chapter 9 were characterized by different local topology and excess free volume, here we also consider interfaces with a different chemical order. It is well known that in the case of amorphous Cu-Zr–alloys, Cu-atoms segregate to the surface at elevated temperatures [163, 164, 165]. When consolidating a glassy nanopowder, which has been subjected to a pre-annealing process, a NG containing interfaces with increased Cu–concentration should form.

10.1 SIMULATION DETAILS

Three dimensional periodic $Cu_{64}Zr_{36}$ nanoglasses with an idealized nanostructure consisting of columnar grains with a hexagonal cross section were constructed by consolidating glassy particles cut from bulk glass. Two types of NGs with the same geometry and same number of atoms ($\approx 5.5{\cdot}10^5$) were generated. In one case a chemically homogeneous glassy powder is used. In the other case we used a glassy powder with Cu–atoms segregated to the surfaces, which was generated by pre-annealing a glassy particle at 800 K (about 0.85 T_g) for 10 ns. Both metallic glass powders, with and without surface segregation, are sintered by applying an external hydrostatic pressure of 3 GPa at 50 K to obtain a nanoglass free of pores. In order to analyze the atomic structure of interfaces in both NGs, the Voronoi tessellation method was applied.

For studying the deformation mechanism of NGs in comparison to a homogeneous BMG ($\approx 1.3{\cdot}10^6$ atoms), the structures have been deformed under uniaxial tension parallel to the z-direction. All structures were deformed at 50 K with a

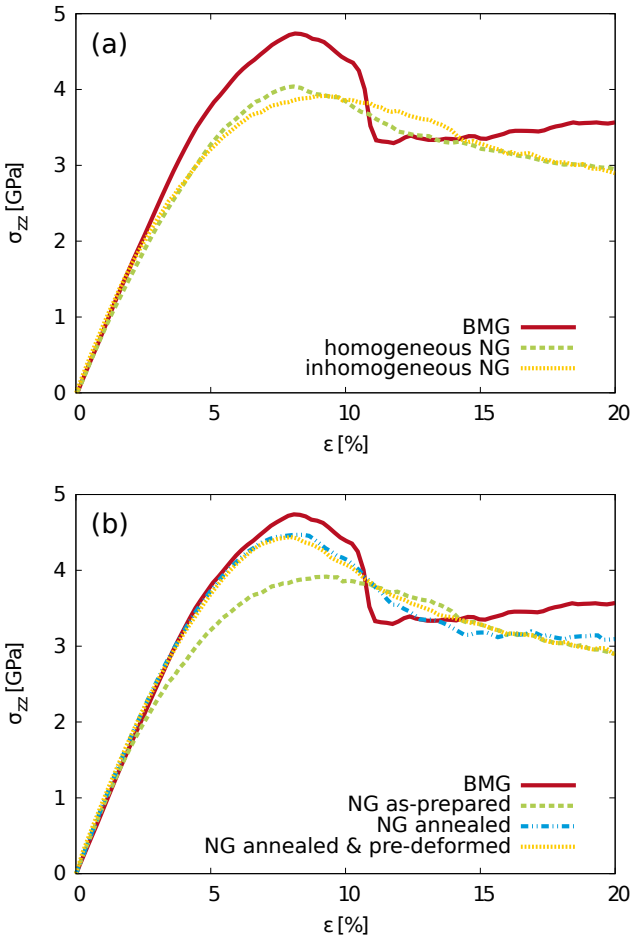

Figure 59: Tensile stress-strain curves for: a) BMG, and as-prepared homogeneous and inhomogeneous NGs; b) BMG, as-prepared, annealed, annealed and pre-deformed inhomogeneous NG, at a constant strain rate of 4×10^7 $1/s$.

constant strain rate of 4×10^7 $1/s$ in z-direction. Periodic boundary conditions were applied in all three dimensions and the pressure in x- and y-direction was adjusted to 0 kbar allowing for lateral contraction.

10.2 DEFORMATION BEHAVIOR OF AS-PREPARED NANOGLASSES

The stress-strain curves for both NGs and the BMG under tensile deformation are plotted in Fig. 59(a). Up to a strain of about 2%, all three curves show a similar slope and, thus, the interfaces have no strong influence on the elastic deformation. The stress at which the curves deviate from a linear behavior is defined to be the yield stress of the samples, which is significantly lower for

both nanoglasses at about 2.4 GPa compared to the bulk glass with a yield stress of approximately 3.3 GPa. The same trend is found for the maximum stress, which is 3.9 GPa for the inhomogeneous NG and 4.0 GPa for the homogeneous NG compared to 4.7 GPa in the case of the BMG. This can be explained by the lower activation barrier for shear transformation zones in the nanoglass interfaces due to a lower population of FI compared to the bulk glass. Cu-centered full icosahedra are VPs with a high packing density [45] and high shear resistance [43] and, therefore, those regions in a glass with a lower content of FIs are easier to deform plastically. This result is supported by an analysis of the atomic scale mechanisms during deformation, which are visualized using the atomic level shear strains. Up to a strain of 8%, where the maximum stress is reached, STZs are only activated in the soft interface regions (see Fig. 60). With increasing strain, in both NGs, multiple embryonic shear bands are formed along the interfaces and eventually start to propagate through the grain interiors. Due to the high number of embryonic shear bands formed in the interfaces, the elastic energy is released homogeneously in the whole sample. Since shear band propagation is driven by the elastic energy [87], the local energy release is not sufficient to accelerate one of the shear bands, so that is goes critical. Consequently, both NGs deform homogeneously in contrast to the BMG, which exhibits localized deformation in one major shear band (see Fig. 60, top). The propagation of one single shear band leads to a significant stress drop in the case of the BMG, which is not observed for the nanoglasses due to the branching into multiple shear bands leading to a more homogeneous deformation. For larger strains the homogeneous sample and the annealed nanoglass show a slight increase in flow stress, which is due to the fact the shear bands have to rotate in the 3-dim. periodic setup and the Schmid factor is decreasing. The flow strain of the as-prepared sample, however, is similar to the annealed and pre-deformed one. In these cases, we observe a strain softening at larger strains, because plastic flow occurs more homogeneously in a network of interpenetrating shear bands.

Besides the homogeneously released elastic energy, shear band propagation is compromised by the intersection of shear bands with different orientation (see Fig. 60). This effect has already been observed in metallic glasses that were pre-deformed by cold rolling [81].

A quantitative interpretation of strain localization has been realized by using the degree of strain localization parameter ψ. A larger ψ value indicates larger fluctuations in the atomic strain and a more localized deformation mode. Comparing the strain localization parameters for the NGs and BMG (see Fig. 61) at a strain of 16%, our observation of a more homogeneous deformation in the NGs is supported. Moreover, the values for both types of NGs are almost identical indicating that the Cu-segregation to the interfaces does not have a significant influence on the deformation behavior.

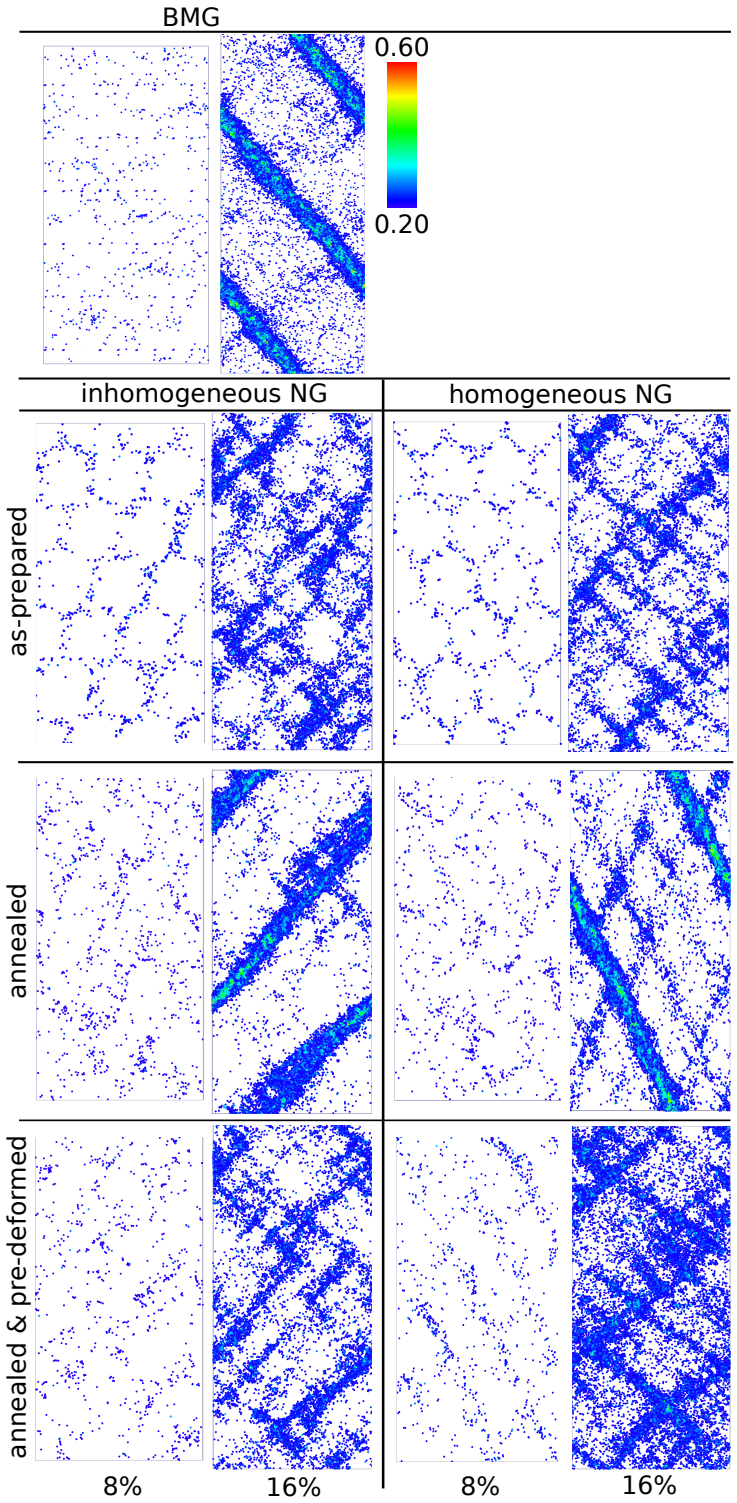

Figure 60: Local atomic shear strain for a inhomogeneous (with Cu-enriched interfaces) and homogeneous (with homogeneous elements distribution) NGs as-prepared, annealed, annealed and pre-deformed in comparison with a BMG, under tensile deformation.

10.3 INFLUENCE OF ANNEALING AND PRE-STRAINING

As shown in the previous chapter, glass-glass interfaces annealed at a temperature close to T_g, are subject to a structural relaxation, involving a partial recovery of the icosahedral SRO. Still, the interface structure after annealing, is characterized by a difference in the icosahedral SRO of about 2 % in comparison to the bulk. These results are in line with experimental observations on pre-induced shear bands produced by indentation [140] or cold rolling [95], where structural disorder is retained in the shear bands even after annealing without strongly affecting the mechanical behavior. Therefore, the questions arises how thermal annealing prior to deformation does affect the plastic deformation mechanisms operating in a NG. In order to answer this question, both types of NGs have been subjected to an annealing process at 700 K (0.75 T_g) for 2 ns. After annealing, the NGs have been cooled down to 50K and subsequently deformed in uniaxial tension following the same procedure as before.

At a strain of 8% shear transformations occur in the interfaces similar to the previous case of non-annealed NGs. When the strain is increased, however, the deformation mechanism changes. In agreement to experimental observation [95] the plastic deformation no longer takes place in a network of multiple shear bands. Instead, the deformation is more localized and at a strain of about 16 %, one dominant shear band is formed. Nevertheless, the plastic deformation mechanism of the annealed NGs deviates from what has been observed for the BMG. The shear band in the annealed NGs is not as well localized as in the BMG. At a strain of 16 % even indications of shear band branching are observed (see Fig. 60), a mechanism which has been reported for BMGs with pre-induced SBs, as well [82]. The same effect is also seen in the ψ-parameter, where the values of the annealed samples are higher than for the as-prepared NGs but not higher as for BMG (see Fig. 61). However, the SRO recovery in the interfaces is slightly more pronounced for the homogeneous NG, which results in a higher ψ-parameter, and therefore, a more localized deformation. Moreover, comparing the stress-strain behavior for the BMG and the annealed NGs (see Fig. 59(b)), the differences are still significant. Therefore, the interfaces in the annealed NGs still can have an impact on plastic deformation.

The next question we address is whether a homogeneous deformation mode can be recovered after annealing. Therefore, the annealed NGs have been pre-loaded to a strain level of 8%, just where the plastic deformation already starts to initiate in the interfaces, but no localized shear bands occurs (see Fig. 60). After unloading to zero strain, the NGs were deformed for a second time. Interestingly, the plastic deformation behavior is almost identical to that before annealing. The NGs undergo plastic deformation mediated by multiple shear bands, uniformly distributed over the sample volume. This is attributed to STZs which affect the short range order and, at a strain of 0.08, occur

mainly in the soft interfaces. This is in good agreement with the ψ-parameters, which nearly shift back to the same values as found for as-prepared NGs. Again, the value for the homogeneous NG is higher indicating stronger shear localization. Consequently, the SRO in the interfaces, which had been recovered during annealing, is damaged during pre-loading and, again, the interfaces act as shear band nucleation sites preventing the plastic deformation to localize in a single shear band as in the case of BMGs or annealed NGs. Analyzing the stress-strain behavior of the different NGs upon tensile deformation (see Fig. 59(b)), we find the annealing process to increase the yield stress as well as the maximum stress. This is due to the recovery of interfacial SRO upon annealing, which leads to an increase in activation barrier for interface-STZs. Interestingly, the annealed and then preloaded NG shows an almost identical stress-strain behavior as the annealed NG, despite the observed differences in deformation mode.

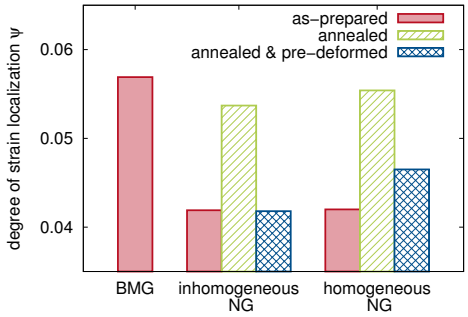

Figure 61: The ψ values for BMG, inhomogeneous and homogeneous NGs, as-prepared, annealed, annealed and pre-deformed at 16% strain.

10.4 SUMMARY

In this chapter, we investigated a new approach to improve the plastic behavior of metallic glasses, namely by producing NGs with microstructural inhomogeneities obtained by powder consolidation. These inhomogeneities or interfaces possess an atomic structure which deviates from the bulk and is characterized by an enhanced free volume, lower SRO and increased potential energy. Under tensile deformation, the NGs exhibit a homogeneous plastic deformation in a highly organized pattern of multiple shear bands, distributed in the whole sample, in contrast to a BMG, where the plastic deformation is confined in one single shear band. We show that shear banding is preferentially initiated in the interfaces or soft regions, and these shear bands can distribute the applied strain more homogeneously. Therefore, it can be anticipated that NGs exhibit an enhanced ductility as compared with BMG. The plasticity of a NG can, therefore, be easily tuned by thermal treatment or prior-deformation. Moreover, by varying the powder particle size and, hence, the interface density, mechanical properties can be modified, as well.

Part VI

CONCLUSION

SUMMARY

The main focus of this thesis was the investigation of atomic structures and mechanical properties of Cu–Zr amorphous alloys, particularly the interplay between the two. The key findings are summarized below.

SIMULATION OF CU-ZR AMORPHOUS ALLOYS

- Fully amorphous metallic glass samples can be synthesized by simulating melt quenching with a cooling rate of 0.01 K/ps. The densities and PRDFs of the computer samples agree well with experimental data.
- Interpenetrating FI-units form extended network structures building up the MRO in Cu-Zr glasses, but there is no percolated backbone of FI clusters in the glasses studied here.
- The higher the degree of cross-linking in the MRO-clusters, the higher the local packing density and the lower the local potential energy.
- The cross-linking is more pronounced in $Cu_{64}Zr_{36}$ glass and the MRO-clusters are larger as compared to the $Cu_{36}Zr_{64}$ glass.
- A higher cooling rate leads to a lower degree of cross-linking and smaller MRO-clusters.
- The CSRO in $Cu_{64}Zr_{36}$ and $Cu_{36}Zr_{64}$ deviates from a statistical alloy; for both alloys the number of Cu-Cu bonds is lower than expected from the global composition while Cu-Zr and Zr-Zr bonds are favored, which is in good agreement with experiments.

INTRINSIC STRAIN LOCALIZATION

- Shear banding is the dominant deformation regime if tensile deformation is simulated at 50 K by applying a strain rate of $10^8\,s^{-1}$, if the sample has free surfaces, and $4 \cdot 10^7\,s^{-1}$, if the sample is fully periodic.
- Strain localization is an intrinsic metallic glass property and even a defect-free sample without free surfaces forms a dominant shear band. Extrinsic stress concentrators are not necessary for the formation of shear bands.

- In the presence of free surfaces, a SB forms in a heterogeneous nucleation process at a free surface, while homogeneous SB nucleation occurs in the absence of free surfaces. The SB nucleation rate is higher for heterogeneous nucleation (between $10^8\,s^{-1}$ and $10^9\,s^{-1}$) than for homogeneous nucleation ($\approx 10^8\,s^{-1}$).
- A SB nucleus forms by the percolation of STZs along a viable shear path. A critical nucleus propagates along a maximum stress plane.
- Local shearing involves the creation of excess volume in a SB, while the surrounding material is densified. This densification is caused by the sudden release of elastic energy at the onset of SB slip allowing the material outside the SB to relax into a different structural configuration with higher packing density.
- In the presence of free surfaces, structural relaxations occur in the SB during deformation.
- There is no intrinsic size effect in the plastic deformation of metallic glasses. Even in nanowires of only 5 nm diameter, plastic deformation is highly localized.
- In amorphous $Cu_{64}Zr_{36}$ nanowires, strain localization most frequently occurs by shear banding, but if several SBs nucleate simultaneously on different slip planes, a neck forms and the material flows.
- The occurrence of shear banding or necking, respectively, does not depend on the sample size.
- The activation free energy and specific volume of a shear transformation zone in $Cu_{64}Zr_{36}$ are independent of the sample size (0.5 eV and $0.3\,nm^3 \approx$ 20 atoms).
- The large homogeneous elongations observed in experimental studies of metallic glass nano-samples are likely related to extrinsic factors such as irradiation damage during FIB milling or heating in the electron beam during in-situ mechanical testing.

CHEMICAL AND TOPOLOGICAL ORDER IN SHEAR BANDS

- The CSRO in $Cu_{64}Zr_{36}$ and $Cu_{36}Zr_{64}$ glass is affected by plastic deformation in a SB: in both alloys the fraction of Cu-Cu- and Zr-Zr-bonds increases, while the fraction of unlike Cu-Zr-bonds decreases. The surrounding matrix is hardly affected.

- In both glassy alloys shear banding involves flow dilatation. In the Cu-rich glass, the increase in free volume is related to a decrease in the total number of densely packed FI clusters. In the Zr-rich glass, the total number of FIs is constant. Here, the destruction of original FIs is fully compensated by newly formed FI clusters, but the new FIs are less densely packed.
- There is no alternative atomic cluster with high packing density in $Cu_{36}Zr_{64}$ glass, which is responsible for the shear stability of the material and which is destroyed upon yielding.
- In the Cu-rich glass, the MRO-clusters built from FI units are damaged in the SB; their size and the degree of cross-linking decreases. In the Zr-rich glass, the MRO in the SB is hardly affected.
- Since both glasses deform by shear banding we conclude that the concept of a network of interpenetrating FI units, which is locally damaged causing strain localization in a SB, is not appropriate to describe the plasticity of Cu-Zr glasses.
- When a deformed sample is annealed at temperatures below T_g, the release of excess volume and the recovery of TSRO are linearly coupled.
- A full recovery of CSRO and TSRO in a SB can only be achieved for annealing temperatures above T_g.
- At 500 K ($\approx 0.55T_g$), collective motion is the only relevant relaxation mechanism. At 800 K ($\approx 0.85T_g$), Cu-nearest neighbor jumps occur in addition to cooperative atomic jumps.
- The number of atoms per jump and the individual atomic displacements are higher at 800 K than at 500 K.
- The collective jumps show characteristics of a chain-type process with mostly linear chains, but at the beginning of annealing jumps involve a large number of atoms in complex clusters or highly branched chains in the SB, similar to flow-like motion in supercooled liquids.
- Our results provide a link between free volume theory, which predicts instantaneous recovery of shear bands at elevated temperatures due to locally increased atomic mobilities like in the supercooled liquid, and experiments, where shear bands recover on time scales in the range of hours: While at the beginning of annealing relaxation mechanisms in a SB resemble processes in supercooled liquids, the fast annihilation of excess volume in this regime causes a rapid increase in the local packing density and after only 20 ns no enhanced diffusivity is found in the shear band anymore. A full recovery on short time scales is, therefore, inhibited.

NANOGLASSES

- Nanoglasses are metallic glasses with microstructural inhomogeneities obtained by powder consolidation.
- Glass-glass interfaces are characterized by a defective short range order and an excess free volume of about 1-2%.
- These interfaces are stable on MD time scales and even after annealing at 800 K ($\approx 0.85 T_g$) the atomic structure of the interface clearly differs from the bulk glass.
- Upon deformation, a soft interface allows for shear band formation at lower stress compared to a bulk glass sample, similar to the shear bands in a pre-deformed metallic glass.
- Under tensile deformation, shear banding is preferentially initiated in the soft interfaces, resulting in a highly organized pattern of multiple shear bands, distributed over the whole sample.
- Multiple shear bands can distribute the applied strain more homogeneously, wherefore we predict that nanoglasses exhibit an enhanced ductility as compared to BMGs.
- The plasticity of a nanoglass can be easily tuned by thermal treatment, pre-deformation, and by varying the powder particle size.

OUTLOOK

The results presented in this thesis raise a number of interesting scientific questions, which could serve as the basis for future studies.

In Chapter 3 and 4 we characterized the chemical and topological order in different Cu-Zr glasses and the changes introduced by plastic deformation. In order to develop universal concepts for the processes causing strain localization in metallic glasses, it is necessary to consider different alloy systems. As a first step towards understanding the structure and properties of multicomponent glasses, it is of particular importance to study changes in the structure of binary alloys when adding a third component, like in recent studies on the Cu-Zr-Al system [30, 166]. Moreover, the differences between metal-metal and metal-metalloid glasses, in which the CSRO is more pronounced [27], might be worthwhile studying.

As already mentioned in Chapter 8, experimental studies revealed that during deformation at low temperatures, nanocrystallites preferentially form inside shear bands [154, 155]. Moreover, Pauly *et al.* observed that the deformation-induced phase transformation increases the ductility of Cu-Zr based bulk metallic glasses [167]. The atomic mechanisms leading to crystallization at temperatures well below the glass transition temperature are still not fully understood. Given the availability of an adequate interatomic potential, which is capable of reproducing the phase diagram of an alloy system as well as the properties of the glassy phases, MD simulations could provide insights how local order, deformation temperature and local strain influence the crystallization kinetics. Moreover, the influence of nanocrystallites on the mechanical properties of Cu-Zr glasses can be studied by deforming Cu-Zr glasses with pre-induced nanocrystallites. In this approach, precipitates of different crystalline phases can be compared and the size, shape and distribution of the crystallites can be easily varied.

The promising results on metallic nanoglasses presented in Part V open a whole new field of glass research. Concerning the mechanical properties of metallic NGs, the most obvious question is whether concepts known from polycrystalline metals can also be applied to amorphous metals: How does grain refinement affect the mechanical properties of NGs? Can the properties of NGs be modified by the enrichment with certain elements in the interfaces? How does the precipitation of second phases, either crystalline or amorphous, alter their mechanical response?

But nanoglasses are not only interesting for their structural properties, they are also candidate materials for functional applications. Recent experimental studies [168] revealed unique magnetic properties of Fe-Sc nanoglasses. The relationship between atomic level structure, structural defects, and electronic and magnetic properties could be investigated using density functional theory calculations.

Oxide nanoglasses are potentially appealing as ionic conductors due to fast diffusion paths provided by the glass-glass interfaces. In lithium ion batteries, where amorphous Si-C-O is investigated as a promising anode material [169], fast diffusion paths along internal interfaces could enable faster lithium intercalation and deintercalation. A combination of density functional theory calculations and large scale molecular dynamics simulations could provide insights in structure-property relationships.

CONTRIBUTIONS

The results presented in Part v, which were published in two articles [A2, A3], originate from a joint project and include data from D. Sopu. For Chapter 9, D. Sopu contributed the sample containing one planar interface and his data on thermal annealing, while my contributions include the structural characterization of the samples, the simulation of plastic deformation and the comparison between interfaces and shear bands. In Chapter 10, the simulation of inhomogeneous nanoglasses and the simulation of annealing and pre-deformation were contributed by D. Sopu, while I simulated the preparation and deformation of homogeneous nanoglasses and the bulk metallic glass.

ERKLÄRUNG – DISCLAIMER

Die vorliegende Arbeit wurde im Zeitraum von Dezember 2007 bis Oktober 2011 im Fachgebiet Materialmodellierung am Institut für Materialwissenschaft der Technischen Universität Darmstadt bei Herrn Prof. Dr. rer. nat. Karsten Albe angefertigt.

Hiermit versichere ich an Eides statt, dass ich die vorliegende Arbeit selbstständig und nur unter Verwendung der angegebenen Hilfsmittel angefertigt habe. Von mir wurde weder an der Technischen Universität Darmstadt noch an einer anderen Hochschule ein Promotionsversuch unternommen.

Darmstadt, den 01. November 2011

Yvonne Ritter

DANKSAGUNG – ACKNOWLEDGMENTS

An dieser Stelle möchte ich mich bei allen bedanken, die mich während der letzten vier Jahre unterstützt und zum Gelingen dieser Arbeit beigetragen haben.

Mein besonderer Dank gilt Prof. Karsten Albe, unter dessen Betreuung ich gelernt habe Probleme als wissenschaftliche Herausforderung zu sehen und an die Relevanz meiner Ergebnisse zu glauben. Vor allem aber bedanke ich mich fuer sein Vertrauen in mich und für die Freiheit meinen eigenen Ideen nachzuforschen.

Prof. Gerhard Wilde danke ich für die Begutachtung meiner Arbeit und dafür, dass er die weite Reise von Münster nach Darmstadt auf sich nimmt.

Ich bedanke mich ganz herzlich bei allen MMs für die einzigartige Arbeitsatmosphäre ("Look at you, you're cool guys!"), die ich in jedem Fall vermissen werde. Danke aber auch für zahlreiche aufschlussreiche Diskussionen über Ikosaeder und Nanodrähte. Special thanks to Daniel Sopu, not only for the successful collaboration on nanoglasses, but also for being in the glass-business with me. Bei Jonathan Schäfer möchte ich mich für das Korrekturlesen dieser Arbeit und die konstruktive Kritik bedanken. Alexander Stukowski danke ich für den individuellen Ovito-Support und seine Unterstützung vor allem zu Beginn meiner Arbeit.

Besonders herzlich möchte ich Renate Hernichel danken für ihre Hilfsbereitschaft in allen organisatorischen Dingen, die moralische Unterstützung, und die Versorgung mit gutem Kaffee.

Zu guter Letzt möchte ich mich bei meinen Eltern bedanken, ohne die ich nicht so weit gekommen wäre, und bei Steffen, für seine Geduld, sein Verständnis, und dafür, dass er von Anfang an wusste, dass alles gut wird.

Teile der vorliegenden Arbeit wurden gefördert durch die Deutsche Forschungsgemeinschaft im Rahmen des Projekts Al-578-6. Rechenzeit wurde zur Verfügung gestellt durch das Forschungszentrum Jülich, das Center for Scientific Computing der Goethe Universität Frankfurt, sowie den Hessischen Hochleistungrechner in Darmstadt. Die Zusammenarbeit mit Prof. Ju Li an der University of Pennsylvania wurde durch ein Doktorandenstipendium des Deutschen Akademischen Austauschdienstes ermöglicht.

Curiculum Vitae

Personal data

Name	Yvonne Ritter
Address	Hoffmannstr. 38 64285 Darmstadt
Email	ritter@mm.tu-darmstadt.de
Date of birth	17. August 1982 Alzenau i. Ufr., Germany

University Education

12/2011	Defense of PhD-Thesis
since 12/2007	**PhD Thesis:** *"Molecular Dynamics Simulations of Structure-Property Rrelationships in Cu–Zr Metallic Glasses"* Materials Modeling Division (Prof. K. Albe), Technische Universität Darmstadt, Germany
05/2007–11/2007	**German Diploma Thesis:** *"Molecular Dynamics Simulation of Deformation Mechanisms in Nanocrystalline FCC Metals"* Materials Modeling Division (Prof. K. Albe), Technische Universität Darmstadt, Germany
10/2002–12/2007	**Studies:** Materials Science, Technische Universität Darmstadt, Germany

Research Experience

12/2007–Present	**Research Associate** (Wissenschaftliche Mitarbeiterin) Materials Modeling Division (Prof. K. Albe), Technische Universität Darmstadt, Germany
01/2010–04/2010	**Visiting Scientist**, Department of Materials Science and Engineering (Prof. Ju Li), University of Pennsylvania, Philadelphia, USA
11/2008–12/2008	**Visiting Scientist**, Division of Materials Physics (Prof. Kai Nordlund), University of Helsinki, Helsinki, Finland

09/2006–12/2006 **Internship**,
Institute of Material Science (Prof. M. Hoffman),
University of New South Wales, Sydney, Australia

School Education

1993–2002 **Secondary School:** Hanns–Seidel–Gymnasium, Hösbach, Germany

06/2002 Graduation from secondary school (*Abitur*),
Hanns–Seidel–Gymnasium, Hösbach, Germany

Peer Reviewed Articles

A1 D. Sopu, K. Albe, Y. Ritter and K. Albe, *From nanoglasses to bulk massive glasses*, Appl. Phys. Lett. **94**, 191911 (2009).

A2 D. Sopu, Y. Ritter, H. Gleiter and K. Albe, *Deformation behavior of bulk and nanostructured metallic glasses studied via molecular dynamics simulations*, Phys. Rev. B **83**, 100202 (2011).

A3 Y. Ritter, D. Sopu, H. Gleiter and K. Albe, *Structure, stability and mechanical properties of internal interfaces in Cu64Zr36-nanoglasses studied by MD simulations*, Acta Mat. **59**, 6588 (2011).

A4 Y. Ritter and K. Albe, *Thermal annealing of shear bands in deformed metallic glasses: Recovery mechanisms in Cu64Zr36 studied by molecular dynamics simulations*, Acta Mat. **59**, 7082 (2011).

A5 Y. Ritter and K. Albe, *Chemical and topological order in shear bands of $Cu_{64}Zr_{36}$ and $Cu_{36}Zr_{64}$ glasses* , (2011), submitted.

A6 Y. Ritter and K. Albe, *Strain localization in amorphous $Cu_{64}Zr_{36}$ nanowires: Molecular dynamics simulations on the influence of size, surface relaxation state and temperature*, submitted.

Other Publications

A7 Y. Ritter, *Molecular dynamics simulation of deformation mechanisms in nanocrystalline fcc metals*, Diplomarbeit (2007).

A8 K. Albe, A. Stukowski, J. Schäfer, Y. Ritter and D. Farkas, *Deformation processes in nanostructured metals and alloys*, Proceedings of the NIC Symposium, FZ Jülich, Germany (2010).

Oral Presentations at International Conferences

Y. Ritter, A. Stukowski and K. Albe, *Molecular dynamics simulation of dislocation nucleation from special and general grain boundaries in fcc metal bicrystals*, TMS Annual Meeting, New Orleans, USA, 2008

Y. Ritter and K. Albe, *Modeling the mechanical properties of bulk metallic glasses with nanoscale inhomogeneities*, DPG Frühjahrstagung, Dresden, Germany, 2009

Y. Ritter and K. Albe, *Deformation mechanisms in amorphous-crystalline nanocomposites*, TMS Annual Meeting, Seattle, USA, 2010

Y. Ritter and K. Albe, *Shear localization in geometrically confined metallic glasses: A molecular dynamics study*, ISMANAM, Zürich, Switzerland, 2010

Poster Presentations at International Conferences

Y. Ritter, A. Stukowski and K. Albe, *Molecular dynamics simulation of dislocation nucleation from special and general grain boundaries in fcc metal bicrystals*, International Workshop on the Plasticity of Nanocrystalline Metals, Bosen, Germany, 2008

Y. Ritter and K. Albe, *Tuning the mechanical properties of bulk metallic glasses by nanoscale precipitates*, Towards Reality in Nanoscale Materials, Levi, Finnland, 2008

Y. Ritter and K. Albe, *Deformation mechanisms in amorphous-crystalline nanocomposites*, Tri-lateral Symposium on "Atomic transport in bulk nanostructured materials and related unique properties", Rouen, France, 2010

Y. Ritter and K. Albe, *Deformation mechanisms in amorphous-crystalline nanocomposites*, MSE 2010 - Materials Science and Engineering, Darmstadt, Germany, 2010

Y. Ritter and K. Albe, *Modeling shear band formation in bulk metallic glasses: Homogeneous vs. heterogeneous nucleation*, MRS Fall Meeting, Boston, USA, 2010

Y. Ritter and K. Albe, *Strain localization on the nanoscale: Deformation mechanisms in amorphous $Cu_{64}Zr_{36}$ nanowires studied by molecular dynamics simulations*, 2nd International Workshop on the Plasticity of Nanocrystalline Metals, Bosen, Germany, 2011

Darmstadt, November 2011

BIBLIOGRAPHY

[1] A. Inoue, K. Ohtera, K. Kita, and T. Masumoto, Jpn. J. Appl. Phys. **27**, L2248 (1988).

[2] A. Inoue, T. Zhang, and T. Masumoto, Mater. Trans. JIM **30**, 965 (1989).

[3] A. Inoue, T. Zhang, and T. Masumoto, Mater. Trans. JIM **31**, 177 (1990).

[4] C. A. Schuh, T. C. Hufnagel, and U. Ramamurty, Acta Mater. **55**, 4067 (2007).

[5] J. Eckert, J. Das, S. Pauly, and C. Duhamel, J. Mater. Res. **22**, 285 (2007).

[6] Y. Zhang, Mater. Sci. Technol. **24**, 379 (2008).

[7] J. H. Li, Y. Dai, Y. Y. Cui, and B. X. Liu, Mat. Sci. Eng. R **72**, 1 (2011).

[8] D. H. Xu, B. Lohwongwatana, G. Duan, W. L. Johnson, and C. Garland, Acta Materialia **52**, 2621 (2004).

[9] W. Klement, R. H. Willens, and P. Duwetz, Nature **187**, 869 (1960).

[10] J. Schroers, Adv. Mater. **22**, 1566 (2010).

[11] A. Peker and W. L. Johnson, Appl. Phys. Lett. **63**, 2342 (1993).

[12] X. H. Lin and W. L. Johnson, J. Appl. Phys. **78**, 6514 (1995).

[13] R. Zallen, *The Physics of amorphous solids* (Wiley-VCH, Weinheim, 1983).

[14] M. D. Ediger, Annu. Rev. Phys. Chem. **51**, 99 (2000).

[15] F. Spaepen and D. Turnbull, Annu. Rev. Phys. Chem. **35**, 241 (1984).

[16] J. Jackle, Rep. Prog. Phys. **49**, 171 (1986).

[17] M. H. Cohen and D. Turnbull, J. Chem. Phys. **31**, 1164 (1959).

[18] D. Turnbull and M. H. Cohen, J. Chem. Phys. **34**, 120 (1961).

[19] D. Turnbull and M. H. Cohen, J. Chem. Phys. **52**, 3038 (1970).

[20] E. Donth, *The glass transition* (Springer, Berlin, 2010).

[21] G. Kumar, D. Rector, R. D. Conner, and J. Schroers, Acta Mater. **57**, 3572 (2009).

[22] M. Goldstein, J. Chem. Phys. **51**, 3728 (1969).

[23] F. H. Stillinger, Science **267**, 1935 (1995).

[24] G. P. Johari and Goldstein.M, J. Chem. Phys. **53**, 2372 (1970).

[25] P. G. Debenedetti and F. H. Stillinger, Nature **410**, 259 (2001).

[26] J. D. Bernal, Nature **183**, 141 (1959).

[27] P. H. Gaskell, Nature **276**, 484 (1978).

[28] D. B. Miracle, Acta Mater. **54**, 4317 (2006).

[29] H. W. Sheng, W. K. Luo, F. M. Alamgir, J. M. Bai, and E. Ma, Nature **439**, 419 (2006).

[30] Y. Q. Cheng, E. Ma, and H. W. Sheng, Phys. Rev. Lett. **102**, 245501 (2009).

[31] Y. Q. Cheng, H. W. Sheng, and E. Ma, Phys. Rev. B **78**, 014207 (2008).

[32] Y. Q. Cheng, A. J. Cao, and E. Ma, Acta Mater. **57**, 3253 (2009).

[33] N. Mattern, P. Jovari, I. Kaban, S. Gruner, A. Elsner, V. Kokotin, H. Franz, B. Beuneu, and J. Eckert, J. Alloys Compd. **485**, 163 (2009).

[34] W. K. Luo, H. W. Sheng, F. M. Alamgir, J. M. Bai, J. H. He, and E. Ma, Phys. Rev. Lett. **92**, 145502 (2004).

[35] M. Li, C. Z. Wang, S. G. Hao, M. J. Kramer, and K. M. Ho, Phys. Rev. B **80**, 184201 (2009).

[36] A. Hirata, P. F. Guan, T. Fujita, Y. Hirotsu, A. Inoue, A. R. Yavari, T. Sakurai, and M. W. Chen, Nat. Mater. **10**, 28 (2011).

[37] A. L. Greer and E. Ma, MRS Bull. **32**, 611 (2007).

[38] M. W. Chen, Annu. Rev. Mater. Res. **38**, 445 (2008).

[39] D. Ma, A. D. Stoica, L. Yang, X. L. Wang, Z. P. Lu, J. Neuefeind, M. J. Kramer, J. W. Richardson, and T. Proffen, Appl. Phys. Lett. **90**, 211908 (2007).

[40] X. J. Liu, X. D. Hui, H. Y. Hou, T. Liu, and G. L. Chen, Phys. Lett. A **372**, 3313 (2008).

[41] F. C. Frank, P. Roy. Soc. Lond. A Mat. **215**, 43 (1952).

[42] F. C. Frank and J. S. Kasper, Acta Crystallogr. **11**, 184 (1958).

[43] Y. Q. Cheng, A. J. Cao, H. W. Sheng, and E. Ma, Acta Mater. **56**, 5263 (2008).

[44] N. Jakse and A. Pasturel, Appl. Phys. Lett. **93**, 113104 (2008).

[45] J. C. Lee, K. W. Park, K. H. Kim, E. Fleury, B. J. Lee, M. Wakeda, and Y. Shibutani, J. Mater. Res. **22**, 3087 (2007).

[46] M. Lee, C. M. Lee, K. R. Lee, E. Ma, and J. C. Lee, Acta Mater. **59**, 159 (2011).

[47] F. Spaepen, Acta Metall. **25**, 407 (1977).

[48] M. L. Falk and J. S. Langer, Phys. Rev. E **57**, 7192 (1998).

[49] S. G. Mayr, Phys. Rev. Lett. **97**, 195501 (2006).

[50] A. S. Argon, Acta Metall. **27**, 47 (1979).

[51] C. A. Schuh, A. C. Lund, and T. G. Nieh, Acta Mater. **52**, 5879 (2004).

[52] E. R. Homer and C. A. Schuh, Acta Mater. **57**, 2823 (2009).

[53] L. Wang, Z. P. Lu, and T. G. Nieh, Scr. Mater. **65**, 759 (2011).

[54] J. S. Harmon, M. D. Demetriou, W. L. Johnson, and K. Samwer, Phys. Rev. Lett. **99**, 135502 (2007).

[55] J. S. Langer, Scr. Mater. **54**, 375 (2006).

[56] W. L. Johnson and K. Samwer, Phys. Rev. Lett. **95**, 195501 (2005).

[57] Y. Shi and M. L. Falk, Scr. Mater. **54**, 381 (2006).

[58] C. E. Packard and C. A. Schuh, Acta Mater. **55**, 5348 (2007).

[59] A. J. Cao, Y. Q. Cheng, and E. Ma, Acta Mater. **57**, 5146 (2009).

[60] B. Yang, M. L. Morrison, P. K. Liaw, R. A. Buchanan, G. Wang, C. T. Liu, and M. Denda, Appl. Phys. Lett. **86**, 141904 (2005).

[61] Y. F. Shi and M. L. Falk, Phys. Rev. B **73**, 214201 (2006).

[62] Q. K. Li and M. Li, Intermetallics **14**, 1005 (2006).

[63] Y. Kawamura, T. Shibata, A. Inoue, and T. Masumoto, Scr. Mater. **37**, 431 (1997).

[64] A. Reger-Leonhard, M. Heilmaier, and J. Eckert, Scr. Mater. **43**, 459 (2000).

[65] H. Kato, Y. Kawamura, A. Inoue, and H. S. Chen, Appl. Phys. Lett. **73**, 3665 (1998).

[66] B. Yang and T. G. Nieh, Acta Mater. **55**, 295 (2007).

[67] M. Calin, J. Eckert, and L. Schultz, Scr. Mater. **48**, 653 (2003).

[68] K. Hajlaoui, A. R. Yavari, A. LeMoulec, W. J. Botta, F. G. Vaughan, J. Das, A. L. Greer, and A. Kvick, J. Non-Cryst. Solids **353**, 327 (2007).

[69] Y. F. Shi and M. L. Falk, Acta Mater. **55**, 4317 (2007).

[70] A. C. Lund and C. A. Schuh, Phil. Mag. Lett. **87**, 603 (2007).

[71] D. C. Hofmann, J. Y. Suh, A. Wiest, G. Duan, M. L. Lind, M. D. Demetriou, and W. L. Johnson, Nature **451**, 1085 (2008).

[72] C. Fan and A. Inoue, Mater. Trans. **38**, 1040 (1997).

[73] C. C. Hays, C. P. Kim, and W. L. Johnson, Phys. Rev. Lett. **84**, 2901 (2000).

[74] C. C. Hays, C. P. Kim, and W. L. Johnson, Mater. Sci. and Eng. A **304**, 650 (2001).

[75] G. He, J. Eckert, W. Loser, and L. Schultz, Nat. Mater. **2**, 33 (2003).

[76] T. G. Nieh and J. Wadsworth, Intermetallics **16**, 1156 (2008).

[77] Y. M. Wang, A. V. Hamza, and T. W. Barbee, Appl. Phys. Lett. **91**, 061924 (2007).

[78] Y. Zhang and A. L. Greer, Appl. Phys. Lett. **89**, 071907 (2006).

[79] Y. M. Wang, J. Li, A. V. Hamza, and T. W. Barbee, Proc. Natl. Acad. Sci. U. S. A. **104**, 11155 (2007).

[80] Y. Yokoyama, J. Non-Cryst. Solids **316**, 104 (2003).

[81] Q. P. Cao *et al.*, Acta Mater. **58**, 1276 (2010).

[82] M. H. Lee, K. S. Lee, J. Das, J. Thomas, U. Kuhn, and J. Eckert, Scr. Mater. **62**, 678 (2010).

[83] L. He, M. B. Zhong, Z. H. Han, Q. Zhao, F. Jiang, and J. Sun, Mater. Sci. Eng. A **496**, 285 (2008).

[84] J. L. Zhang, H. B. Yu, J. X. Lu, H. Y. Bai, and C. H. Shek, Appl. Phys. Lett. **95**, 071906 (2009).

[85] X. D. Wang, Q. P. Cao, J. Z. Jiang, H. Franz, J. Schroers, R. Z. Valiev, Y. Ivanisenko, H. Gleiter, and H. J. Fecht, Scr. Mater. **64**, 81 (2011).

[86] C. A. Volkert, A. Donohue, and F. Spaepen, J. Appl. Phys. **103**, 083539 (2008).

[87] C. Q. Chen, Y. T. Pei, and J. T. M. De Hosson, Acta Mater. **58**, 189 (2010).

[88] H. Guo, P. F. Yan, Y. B. Wang, J. Tan, Z. F. Zhang, M. L. Sui, and E. Ma, Nat. Mater. **6**, 735 (2007).

[89] D. C. Jang and J. R. Greer, Nat. Mater. **9**, 215 (2010).

[90] J. H. Luo, F. F. Wu, J. Y. Huang, J. Q. Wang, and S. X. Mao, Phys. Rev. Lett. **104**, 215503 (2010).

[91] B. E. Schuster, Q. Wei, T. C. Hufnagel, and K. T. Ramesh, Acta Mater. **56**, 5091 (2008).

[92] A. Dubach, R. Raghavan, J. F. Loffler, J. Michler, and U. Ramamurty, Scr. Mater. **60**, 567 (2009).

[93] X. L. Wu, Y. Z. Guo, Q. Wei, and W. H. Wang, Acta Mater. **57**, 3562 (2009).

[94] Y. F. Shi, Appl. Phys. Lett. **96**, 121909 (2010).

[95] W. H. Jiang, F. E. Pinkerton, and M. Atzmon, Acta Mater. **53**, 3469 (2005).

[96] J. Jing, A. Kramer, R. Birringer, H. Gleiter, and U. Gonser, J. Non-Cryst. Solids **113**, 167 (1989).

[97] M. P. Allen and D. J. Tildesley, *Computer Simulation of Liquids* (Clarendon Press, Oxford, 1986).

[98] D. C. Rapaport, *The art of molecular dynamics simulation* (Cambridge University Press, Cambridge, 1995).

[99] M. J. Buehler, A. Hartmaier, H. J. Gao, M. Duchaineau, and F. F. Abraham, Comput. Method. Appl. M. **193**, 5257 (2004).

[100] S. Plimpton, J.Comput. Phys. **117**, 1 (1995).

[101] N. W. Ashcroft and N. D. Mermin, *Solid State Physics* (Holt, Reinhart & Winston, New York, 1976).

[102] S. M. Foiles, M. I. Baskes, and M. S. Daw, Phys. Rev. B **33**, 7983 (1986).

[103] M. S. Daw and M. I. Baskes, Phys. Rev. B **29**, 6443 (1984).

[104] M. W. Finnis and J. E. Sinclair, Phil. Mag. A **50**, 45 (1984).

[105] M. I. Mendelev, D. J. Sordelet, and M. J. Kramer, J. Appl. Phys. **102**, 043501 (2007).

[106] G. J. Ackland and V. Vitek, Phys. Rev. B **41**, 41 (1990).

[107] M. I. Mendelev, D. K. Rehbein, R. T. Ott, M. J. Kramer, and D. J. Sordelet, J. Appl. Phys. **102**, 093518 (2007).

[108] H. Zhu and R. S. Averback, Phys. Rev. B **51**, 15559 (1995).

[109] H. J. C. Berendsen, J. P. M. Postma, W. F. van Gunsteren, A. DiNola, and J. R. Haak, J. Chem. Phys. **81**, 3684 (1984).

[110] Y. Q. Cheng and E. Ma, Prog. Mater. Sci. **56**, 379 (2011).

[111] H. S. Chen, Rep. Prog. Phys. **43**, 353 (1980).

[112] G. Z. Voronoi, J. reine angew. Math. **134**, 199 (1908).

[113] W. Brostow, M. Chybicki, R. Laskowski, and J. Rybicki, Phys. Rev. B **57**, 13448 (1998).

[114] O. Gedeon and M. Liska, J. Non-Cryst. Solids **303**, 246 (2002).

[115] S. G. Hao *et al.*, Phys. Rev. B **79**, 104206 (2009).

[116] K. W. Park, J. I. Jang, M. Wakeda, Y. Shibutani, and J. C. Lee, Scr. Mater. **57**, 805 (2007).

[117] F. Shimizu, S. Ogata, and J. Li, Mater. Trans. **48**, 2923 (2007).

[118] A. Stukowski, Model. Simul. Mater. Sci. **18**, 015012 (2010).

[119] M. I. Mendelev, M. J. Kramer, R. T. Ott, and S. D. J., Phil. Mag. **89**, 109 (2009).

[120] Y. Q. Cheng and E. Ma, Appl. Phys. Lett. **93**, 051910 (2008).

[121] C. A. Angell, Science **267**, 1924 (1995).

[122] C. A. Angell, J. Non-Cryst. Solids **354**, 4703 (2008).

[123] C. A. Angell, Mrs Bulletin **33**, 544 (2008).

[124] H. S. Chen and Y. Waseda, Phys. Status Solidi A **51**, 593 (1979).

[125] D. Ma, A. D. Stoica, X. L. Wang, Z. P. Lu, M. Xu, and M. Kramer, Phys. Rev. B **80**, 014202 (2009).

[126] F. Delogu, Phys. Rev. B **79**, 184109 (2009).

[127] J. P. Hirth and J. Lothe, *Theory of dislocations*, 2nd ed. (Wiley, New York, 1982).

[128] H. Van Swygenhoven and J. R. Weertman, Mater. Today **9**, 24 (2006).

[129] F. Delogu, Phys. Rev. Lett. **100**, 255901 (2008).

[130] P. F. Thomason, Acta Metall. **33**, 1087 (1985).

[131] Z. F. Zhang, G. He, J. Eckert, and L. Schultz, Phys. Rev. Lett. **91**, 045505 (2003).

[132] J. E. Lennard-Jones, Z. Kristallogr. **75**, 215 (1930).

[133] R. Shuttleworth, Proc. Phys. Soc. A **63**, 444 (1950).

[134] R. . C. Cammarata and K. Sieradzki, Annu. Rev. Mater. Sci. **24**, 215 (1994).

[135] M. Zink, K. Samwer, W. L. Johnson, and S. G. Mayr, Phys. Rev. B **73**, 172203 (2006).

[136] Q. K. Li and M. Li, Appl. Phys. Lett. **88**, 241903 (2006).

[137] N. P. Bailey, J. Schiotz, and K. W. Jacobsen, Phys. Rev. B **73**, 064108 (2006).

[138] C. E. Lekka, A. Ibenskas, A. R. Yavari, and G. A. Evangelakis, Appl. Phys. Lett. **91**, 214103 (2007).

[139] C. M. Lee, K. W. Park, B. J. Lee, Y. Shibutani, and J. C. Lee, Scr. Mater. **61**, 911 (2009).

[140] S. Xie and E. P. George, Acta Mater. **56**, 5202 (2008).

[141] C. A. Pampillo, Scripta Metall. **6**, 915 (1972).

[142] K. Hajlaoui, T. Benameur, G. Vaughan, and A. R. Yavari, Scr. Mater. **51**, 843 (2004).

[143] K. D. Krishnanand and R. W. Cahn, Scripta Metall. **9**, 1259 (1975).

[144] Y. L. Xu, H. Hahn, and J. G. Li, Intermetallics **18**, 2039 (2010).

[145] C. Nagel, K. Ratzke, E. Schmidtke, and F. Faupel, Phys. Rev. B **60**, 9212 (1999).

[146] A. I. Taub and F. Spaepen, Acta Metall. **28**, 1781 (1980).

[147] F. Birch, J. Geophys. Res. **57**, 227 (1952).

[148] D. C. Wallace, *Thermodynamics of Crystals* (John Wiley & Sons, Inc., New York, 1972).

[149] O. Haruyama and A. Inoue, Appl. Phys. Lett. **88**, 131906 (2006).

[150] C. Donati, J. F. Douglas, W. Kob, S. J. Plimpton, P. H. Poole, and S. C. Glotzer, Phys. Rev. Lett. **80**, 2338 (1998).

[151] D. Caprion, J. Matsui, and H. R. Schober, Phys. Rev. Lett. **85**, 4293 (2000).

[152] F. Faupel, W. Frank, M. P. Macht, H. Mehrer, V. Naundorf, K. Ratzke, H. R. Schober, S. K. Sharma, and H. Teichler, Rev. Mod. Phys. **75**, 237 (2003).

[153] C. Gaukel and H. R. Schober, Solid State Commun. **107**, 1 (1998).

[154] J. J. Kim, Y. Choi, S. Suresh, and A. S. Argon, Science **295**, 654 (2002).

[155] G. Wilde and H. Rosner, Appl. Phys. Lett. **98**, 251904 (2011).

[156] Q. Y. Zhou, A. S. Argon, and R. E. Cohen, Polymer **42**, 613 (2001).

[157] H. S. Kim, Y. Estrin, and M. B. Bush, Acta Mater. **48**, 493 (2000).

[158] A. P. Sutton and R. W. Balluffi, *Interfaces in Crystalline Materials* (Oxford Science Publications, Oxford, 1996).

[159] H. Gleiter, Acta Mater. **56**, 5875 (2008).

[160] D. Sopu, K. Albe, Y. Ritter, and H. Gleiter, Appl. Phys. Lett. **94**, 191911 (2009).

[161] D. Wolf, Acta Metall. Mater. **38**, 791 (1990).

[162] J. Fang, X. Wang, F. Jiang, J. Sun, H. Hahn, and H. Gleiter, unpublished (2011).

[163] M. Kilo, M. Hund, G. Sauer, A. Baiker, and A. Wokaun, J. Alloys Compd. **236**, 137 (1996).

[164] J. Bukowska, A. Kudelski, and M. Janik-Czachor, Chem. Phys. Lett. **268**, 481 (1997).

[165] R. Novakovic, M. L. Muolo, and A. Passerone, Surf. Sci. **549**, 281 (2004).

[166] H. Z. Fang, X. Hui, G. L. Chen, and Z. K. Liu, Appl. Phys. Lett. **94**, 091904 (2009).

[167] S. Pauly, S. Gorantla, G. Wang, U. Kuhn, and J. Eckert, Nat. Mater. **9**, 473 (2010).

[168] R. Witte, Magnetic phenomena in Fe-Sc nanoglasses, Diplomarbeit, 2011.

[169] P. Colombo, G. Mera, R. Riedel, and G. D. Soraru, J. Am. Ceram. Soc. **7**, 1805 (2010).